J. Fluid Mech. (2011), *vol.* 688, *pp.* 461–492.
doi:10.1017/jfm.2011.392

The large-scale flow structure in turbulent rotating Rayleigh–Bénard convection

Stephan Weiss and Guenter Ahlers†

Department of Physics, University of California, Santa Barbara, CA 93106, USA

(Received 2 June 2011; revised 26 July 2011; accepted 11 September 2011;
first published online 1 November 2011)

We report on the influence of rotation about a vertical axis on the large-scale circulation (LSC) of turbulent Rayleigh–Bénard convection in a cylindrical vessel with aspect ratio $\Gamma \equiv D/L = 0.50$ (where D is the diameter and L the height of the sample). The working fluid is water at an average temperature $T_{av} = 40\ ^\circ\mathrm{C}$ with a Prandtl number $Pr = 4.38$. For rotation rates $\Omega \lesssim 1$ rad s^{-1}, corresponding to inverse Rossby numbers $1/Ro$ between 0 and 20, we investigated the temperature distribution at the sidewall and from it deduced properties of the LSC. The work covered the Rayleigh-number range $2.3 \times 10^9 \lesssim Ra \lesssim 7.2 \times 10^{10}$. We measured the vertical sidewall temperature gradient, the dynamics of the LSC and flow-mode transitions from single-roll states (SRSs) to double-roll states (DRSs). We found that modest rotation stabilizes the SRSs. For modest $1/Ro \lesssim 1$ we found the unexpected result that the vertical LSC plane rotated in the prograde direction (i.e. faster than the sample chamber), with the rotation at the horizontal midplane faster than near the top and bottom. This differential rotation led to disruptive events called half-turns, where the plane of the top or bottom section of the LSC underwent a rotation through an angle of 2π relative to the main portion of the LSC. The signature of the LSC persisted even for large $1/Ro$ where Ekman vortices are expected. We consider the possibility that this signature actually is generated by a two-vortex state rather than by a LSC. Whenever possible, we compare our results with those for a $\Gamma = 1$ sample by Zhong & Ahlers (*J. Fluid Mech.*, vol. 665, 2010, pp. 300–333).

Key words: Bénard convection, convection

1. Introduction

Thermal convection occurs in a fluid heated from below (Rayleigh–Bénard convection, RBC) whenever it is exposed to a sufficiently large temperature gradient. The relevance of this phenomenon to natural and industrial processes was discussed in a previous publication (Weiss & Ahlers 2011*a*). In this paper we focus on convection in a simple geometry, namely a right-circular cylinder of height L and diameter D with aspect ratio $\Gamma \equiv D/L = 0.50$. For a sufficiently large temperature difference $\Delta T \equiv T_b - T_t$ (T_b and T_t are the temperatures at the sample bottom and top, respectively) the heat is transported by turbulent fluid motion from the bottom to the top plate (for a review, see e.g. Ahlers, Grossmann & Lohse 2009; Ahlers 2009; Lohse & Xia 2010). Thermal boundary layers (BLs) exist close to the top and bottom

† Email address for correspondence: guenter@physics.ucsb.edu

plates; they are characterized by very large vertical temperature gradients, whereas the average temperature gradient in the bulk is an order of magnitude or more smaller. Warm (cold) fluid volumes, so called 'plumes', originate from the bottom (top) BL, rise (sink) due to their lower (higher) density to the top (bottom) plate and in this way contribute to the driving of the fluid motion. Temperature and velocity measurements have shown that the plume motion and the associated overall fluid flow often organize themselves into a large-scale circulation (LSC), similar to a single (albeit vigorously fluctuating) convection roll.

The LSC shows a variety of different dynamics, such as cessations and fast rotations (Brown, Nikolaenko & Ahlers 2005; Brown & Ahlers 2006*b*; Xi & Xia 2007) or torsional and sloshing oscillations (Funfschilling & Ahlers 2004; Funfschilling, Brown & Ahlers 2008; Xi *et al.* 2009; Brown & Ahlers 2009). Recently we completed a detailed study of the heat transport and the LSC in a cylindrical sample with $\Gamma = 0.50$ (Weiss & Ahlers 2011*b*). For that case the LSC shows interesting transitions between a state where a single convection roll is replaced for a short time by two counter-rotating rolls, one on top of the other (Xi & Xia 2008*b*). Here we investigate the effect of rotating such a sample about a vertical axis. We already presented results and their interpretation for the heat transport in the presence of rotation (Weiss & Ahlers 2011*a*). Here we focus on the properties of the LSC and its dynamics.

Based on the Navier–Stokes and the heat equation one can identify two-dimensionless parameters that contribute to the definition of the state of the system. These are the Rayleigh number

$$Ra = \frac{g\alpha \Delta T L^3}{\nu\kappa} \tag{1.1}$$

and the Prandtl number

$$Pr = \frac{\nu}{\kappa}. \tag{1.2}$$

Here α is the isobaric thermal expansion coefficient, ν the kinematic viscosity, κ the thermal diffusivity and g the gravitational acceleration. In addition, the geometry is characterized by the aspect ratio Γ. The rotation rate Ω (in rad s^{-1}) is expressed in terms of the dimensionless inverse Rossby number

$$1/Ro = \frac{2\Omega}{\sqrt{g\alpha \Delta T/L}} \tag{1.3}$$

which represents the ratio between the Coriolis and the buoyancy forces. Owing to its proportionality to Ω it is a convenient parameter describing the strength of the rotation. Also frequently encountered is the Ekman number $Ek = \nu/(L^2\Omega)$ which is an estimate of the ratio between the viscous and the Coriolis forces. The Taylor number $Ta = (2/Ek)^2$ has also been used.

For non-rotating RBC it is believed that the heat transport is limited by the thickness and the stability of the thermal BLs close to the plates (Malkus 1954), and that, at least for modest to large Pr, the actual flow field in the bulk and the aspect ratio have only a minor influence (Ciliberto, Cioni & Laroche 1996; Xia & Lui 1997; Xu, Bajaj & Ahlers 2000; Funfschilling *et al.* 2005; Nikolaenko *et al.* 2005; Sun *et al.* 2005*a*) (see, however, Bailon-Cuba, Emran & Schumacher 2010 for $Pr = 0.7$ and van der Poel, Stevens & Lohse 2011 for the two-dimensional case). However, it was shown, for instance by Xi & Xia (2008*b*) and Weiss & Ahlers (2011*b*), that the flow field inside the bulk is influenced very much by a change of Γ. For example, while for

$\Gamma = 1$ the LSC has a relatively constant amplitude, shows slow azimuthal diffusion, periodic oscillations and loses its coherent structure only once in a while (cessation), for $\Gamma = 0.50$ and smaller, fluctuations of the strength and the orientation of the LSC become much larger and flow-mode transitions to a double-roll state (DRS) occur.

For small and moderate rotation rates (small $1/Ro$), the formation of vortices leads to Ekman pumping, an effect which extracts hot (cold) fluid from the bottom (top) thermal BL and transports it deep into the bulk region, increasing in this way the heat transport (Rossby 1969; Kunnen 2008; Liu & Ecke 2009; Zhong *et al.* 2009; Stevens *et al.* 2009; Weiss *et al.* 2010; Weiss & Ahlers 2011*a*). However, this effect occurs only above a threshold $1/Ro_c$ (Stevens *et al.* 2009; Weiss & Ahlers 2011*a*), which depends on the aspect ratio Γ (Weiss *et al.* 2010). As reported by Weiss *et al.* (2010) and Weiss & Ahlers (2011*a*), a two-dimensional Ginzburg–Landau-like model that describes the relation between the local vortex density A and $1/Ro$ can be used to explain why in finite-sized containers a minimum $1/Ro_c \propto 1/\Gamma > 0$ has to be exceeded before vortices, and thus heat-transport enhancement, occur.

A detailed investigation of rotating turbulent convection for $\Gamma = 1$ was presented by Zhong & Ahlers (2010). Among other phenomena, they found (in qualitative agreement with earlier work by Hart, Kittelman & Ohlsen (2002) and Kunnen, Clercx & Geurts (2008)) a retrograde rotation of the LSC and an increase of the frequency of cessations with increasing rotation rates.

In this paper we present a detailed investigation of the effect of rotation on turbulent RBC in a cylindrical container of aspect ratio $\Gamma = 0.50$. Our previous work (Weiss & Ahlers 2011*a*) about the influence of rotation on the heat transport in this system revealed two different phase transitions that were visible in the Nusselt number measurements. In the present paper we focus on the LSC. We explored properties of the flow field by measuring the temperature at 24 points along the sidewall. Major and surprising results include prograde rotation of the LSC plane at modest $1/Ro$, a differential flow at the sidewall that leads to partial ruptures of the LSC (so-called half-turns) and a stabilization of the LSC associated with a reduction of flow-mode transitions from a single-roll state (SRS) to a DRS and back again. We found that the periodic azimuthal temperature variation characteristic of the LSC persists up to unexpectedly large rotation rates corresponding to $1/Ro \simeq 20$. However, it was shown by Stevens *et al.* (2011*b*) that, at least for $Ra = 2.9 \times 10^8$ and $1/Ro = 3.33$, there are only two vortices in a $\Gamma = 0.50$ sample, one coming from the cold top and the other from the warm bottom BL. Such a structure presumably would also lead to a sinusoidal azimuthal temperature variation, similar to that characteristic of the LSC. We were unable to distinguish experimentally between these two phenomena.

The next section describes very briefly the experimental set-up and explains the sidewall temperature measurements and their analysis. Section 4 shows measurements of the temperature gradient at the side but far away from top and bottom BLs. The influence of rotation on the LSC is discussed in § 5. This includes a short discussion of the existence of the LSC and of the influence of rotation on the flow-mode transitions from a SRS to a DRS. Next the dynamics of the LSC, such as its diffusive random motion, the number of flow-transition events, the rotation rate of the LSC plane and its bent shape are examined. The article ends with a short summary.

Run	ΔT (K)	$10^{-9}Ra$	$Ro\ \Omega$ (rad s^{-1})	Run	ΔT (K)	$10^{-9}Ra$	$Ro\ \Omega$ (rad s^{-1})
E12	0.50	2.28	0.0311	E15	3.98	17.98	0.0874
E13	1.00	4.51	0.0437	E16	7.95	35.9	0.124
E14	1.99	9.00	0.0618	E17	15.88	71.7	0.175

TABLE 1. Parameters for the experimental runs. For all cases, $Pr = 4.38$, $T_{av} \equiv (T_b + T_t)/2 = 40$ °C, $Ek \times \Omega = 2.73 \times 10^{-6}$ rad s^{-1} and $Ta/\Omega^2 = 1.46 \times 10^{11}$ s^2 rad^{-2}. The last column gives the product $(Ro\,\Omega)$, which is a constant material parameter for a given experimental run.

2. Experimental set-up and data analysis

2.1. *Convection apparatus*

The experimental set-up was the same as that already described as the 'Medium Convection Apparatus' (MCA) by Weiss & Ahlers (2011*b*) and was mounted on a rotating table as described by Zhong & Ahlers (2010). The present experiment was conducted with a sample of aspect ratio $\Gamma = 0.50$ as described by Weiss & Ahlers (2011*a*). Thus, we give only a few brief details.

The fluid for all experiments was water at an average temperature $T_{av} \equiv (T_b + T_t)/2 = 40$ °C resulting in $Pr = 4.38$. The fluid was confined at the top and bottom by copper plates. Five thermistors were incorporated in each plate. In the lateral direction the fluid was confined by a Plexiglas tube of inner diameter $D = 24.77$ cm and appropriate height so that the top and bottom plate were separated by $L = D/\Gamma = 49.5$ cm. The vertical viscous diffusion time $\tau_\kappa \equiv L^2/\nu$ of the sample was 7.0×10^5 s. Various thermal shields prevented parasitic heat losses.

For measurements of the sidewall temperature distribution, 24 thermistors were place from the outside into blind holes in the sidewall as first described by Brown *et al.* (2005). At each of three horizontal circles at heights $z = -L/4$, 0 and $L/4$ away from the midplane of the cell, $N_T = 8$ thermistors were equally distributed azimuthally. Each thermistor was embedded in thermal paste inside the sidewall so that the distance between the thermistor and the fluid was not more than 1 or 2 mm. The five thermistors in the top and bottom plate were calibrated outside the apparatus with a precision of 1 mK against a Hart Scientific Model 5626 platinum resistance thermometer, as described by Zhong & Ahlers (2010). The sidewall thermistors were calibrated inside the apparatus against the top and bottom plate thermistors. During the experiment, the temperatures at the top and bottom plate were held constant. Experiments were performed for six different Ra in the range of $2.3 \times 10^9 < Ra < 7.2 \times 10^{10}$ and for up to 35 different rotation rates at a given Ra. Table 1 lists the runs discussed in this paper.

During a typical experimental run, at constant ΔT and Ω all thermistors were read every 3.2 s or so for at least half a day. For data evaluation the first readings were discarded to avoid transients. Since only the rotation rate Ω was changed slightly between two successive experiments, most of the time it was sufficient to discard only the first hour.

2.2. *Measurement of LSC properties*

The 24 thermistors embedded in the sidewall allow the investigation of certain characteristics of the turbulent flow close to that wall at three different heights. This includes especially some aspects of the structure and the dynamics of the LSC. As

shown previously (Brown *et al.* 2005; Brown & Ahlers 2006*b*), the orientation and strength of the LSC can be determined by fitting the function

$$T_{f,k} = T_{w,k} + \delta_k \cos\left(\frac{2\mathrm{i}\pi}{N_T} - \theta_k\right) \tag{2.1}$$

to each set of the N_T temperatures $T_{i,k}$ at heights $-L/4$, 0 and $L/4$. Here the subscript 'i' denotes the azimuthal location of the thermistors and 'k' denotes the vertical location and can take values 'b' (bottom, $z = -L/4$), 'm' (middle, $z = 0$) and 't' (top, $z = L/4$). The amplitude δ_k and the phase θ_k are measures for the strength and the orientation of the LSC. The constant $T_{w,k}$ is the mean temperature at the sidewall and at the vertical position k.

By following the time evolution of the strength δ_k and orientation θ_k of a convection roll at a single vertical level, one can determine aspects of its dynamics including azimuthal diffusion, rapid rotation events and cessations (Brown *et al.* 2005; Brown & Ahlers 2006*b*). With thermistor rows at three vertical positions it is possible to observe additional features. These include the torsional oscillations (Funfschilling & Ahlers 2004; Funfschilling *et al.* 2008; Zhou *et al.* 2009; Brown & Ahlers 2009) of the SRS where one roll extends from the top to the bottom of the cell, as well as transitions from a SRS to a DRS where two counter-rotating rolls are one on top of the other (Xi & Xia 2008*b*; Weiss & Ahlers 2011*b*). In the latter example the top and the bottom thermistors can detect both rolls, characterized by $\delta_b \approx \delta_t$ and $\theta_b - \theta_t \approx \pi$. In this case the amplitude of the middle thermistor row δ_m would be small.

Although (2.1) under many situations provides a good fit to the eight temperatures measured by the thermometers at a given height k, these measurements contain more information than the three parameters determined from this fit. Thus, in a previous publication (Brown & Ahlers 2007) the time-averaged deviations of the $T_{i,k}$ from the fitted function $T_{f,k}$ were reported as a function of the azimuthal orientation of each thermometer relative to θ_k and analysed for their higher-harmonic contents. Similarly, root-mean-square (r.m.s.) fluctuations about the mean temperature profile were examined. In other publications (Stevens *et al.* 2009; Zhong & Ahlers 2010) the time-averaged r.m.s. fluctuations

$$\langle\sigma_{f,k}\rangle = \left\langle \left(\frac{1}{N_T}\sum_{i=1}^{N_T}(T_{i,k} - T_{f,k})^2\right)^{1/2}\right\rangle_t \tag{2.2}$$

about the fit of (2.1) were compared with the time-averaged amplitude $\langle\delta_k\rangle$ in order to assess the prominence of the LSC. For $\langle\delta_k\rangle$ well above $\langle\sigma_{f,k}\rangle$ the LSC was expected to be well established; but when $\langle\delta_k\rangle$ approached $\langle\sigma_{f,k}\rangle$ as a parameter was varied, the existence of the LSC could no longer be assured.

An important property of the LSC missed by (2.1) is a periodic displacement of the LSC circulation plane away from the vertical centreline of a sample with $\Gamma = 1$ which was discovered by Xi *et al.* (2009) (see also Zhou *et al.* 2009) and named the 'sloshing mode'. By virtue of its symmetry this mode is missed completely by a fit of (2.1) to the eight $T_{i,k}$. In order to detect it, Brown & Ahlers (2009) computed the three non-vanishing sinusoidal Fourier amplitudes $B_{k,j}$, $j = 2, 3, 4$ of the deviations of the sidewall temperatures from the fit of (2.1). The coefficients of the fundamental mode $A_{k,1}$ (the lowest cosine coefficient) and $B_{k,1}$ are of course contained already in the fit parameters of (2.1).

Recently it was advocated by Stevens, Clercx & Lohse (2011*a*) that a complete Fourier analysis of the data should be carried out in order to extract the maximum

information. Such an analysis had been carried out before using data from direct numerical simulation (DNS) by Kunnen *et al.* (2008). Thus, for our case of eight thermometers, we computed the coefficients of the lowest four Fourier modes from the $N_T = 8$ temperatures $T_{k,i}$ at a given k (after having subtracted their mean $T_{w,k}$). This yielded all eight Fourier coefficients $A_{k,j}$ (the cosine coefficients) and $B_{k,j}$ (the sine coefficients), $j = 1, \ldots, 4$ for the case where there are eight temperatures. From these coefficients we determined the 'energy' $E_{k,j}(t) = A_{k,j}^2 + B_{k,j}^2$ for each mode $j = 1, \ldots, N_T/2$. The total Fourier energy is then $E_{k,tot}(t) = \sum_{j=1}^{N_T/2} E_{k,j}(t)$. We note that $E_{k,1}(t) = \delta_k^2(t)$, and that (by Parseval's theorem or Rayleigh's identity) $E_{k,tot}(t)$ is equal to the variance $\sigma_k^2 = (1/N_T)\sum_{i=1}^{N_T} (T_{i,k} - T_{w,k})^2$ of the data. The LSC orientation is given by $\theta_k = \arctan(B_{k,1}/A_{k,1})$.

Stevens *et al.* (2011*a*) suggested further that the parameter

$$S_k(t) = MAX\left[\left(\frac{E_{k,1}/E_{tot} - 1/(N_T/2)}{1 - 1/(N_T/2)}\right), 0\right] \tag{2.3}$$

can be used to assess whether the LSC dominates over fluctuations, or whether its very existence is in question. They note that $S_k = 1$ when all of the Fourier energy is contained in the fundamental mode associated with the LSC, and that $S_k = 0$ when the energy is evenly distributed over all modes as it would be if the $T_{i,k}$ are due to random fluctuations. In the analysis of the present data we use either (2.1) or the Fourier analysis, depending on the purpose at hand.

In addition to the time-dependent (and fluctuating) quantities $E_{k,j}(t)$ and $S_k(t)$, time-averaged quantities are also useful for characterizing a particular convecting state. Thus, when appropriate we also compute the time averages $\langle E_{k,j}\rangle$, $\langle E_{k,tot}\rangle$, and

$$\bar{S}_k = MAX\left[\left(\frac{\langle E_{k,1}\rangle/\langle E_{k,tot}\rangle - 1/(N_T/2)}{1 - 1/(N_T/2)}\right), 0\right]. \tag{2.4}$$

3. Nusselt-number measurements

Measurements of the heat transport, in the form of the dimensionless Nusselt number, for the experiments described in this paper were reported in detail by Weiss & Ahlers (2011*a*). Here we want to give a short summary of those data to better link the flow structures presented in the present paper with the *Nu* results.

Figure 1 shows the reduced Nusselt number $Nu/Nu(0)$ as a function of $1/Ro$ for different Ra. For the case here, with aspect ratio $\Gamma = 0.50$, one can distinguish four different ranges of $1/Ro$ that differ from each other by different slopes $\partial Nu/\partial(1/Ro)$. While in range I Nu increases monotonically with $1/Ro$, in range II Nu increases much less (for small Ra) or decreases monotonically (for larger Ra) with increasing $1/Ro$. A similar behaviour, but with a somewhat smaller Nu increase in range I, was also observed for $\Gamma = 1$ and relatively large Ra (Zhong & Ahlers 2010). The transition point between ranges I and II is identified as $1/Ro_0$. In range III enhancements of Nu are observed, with Nu reaching its maximum values near $1/Ro \approx 3$–5 and decreasing from there on (range IV). The sharp transition between ranges II and III at $1/Ro_c = 0.85$ can be explained by the formation of vortices close to the thermal BLs that, owing to the finite lateral size of the container, cannot form at smaller $1/Ro$ (Weiss & Ahlers 2011*a*). Within these vortices, Ekman suction takes place and transports fluid out of the hot (cold) thermal BL at the bottom (top) plate and thus enhances the heat transport.

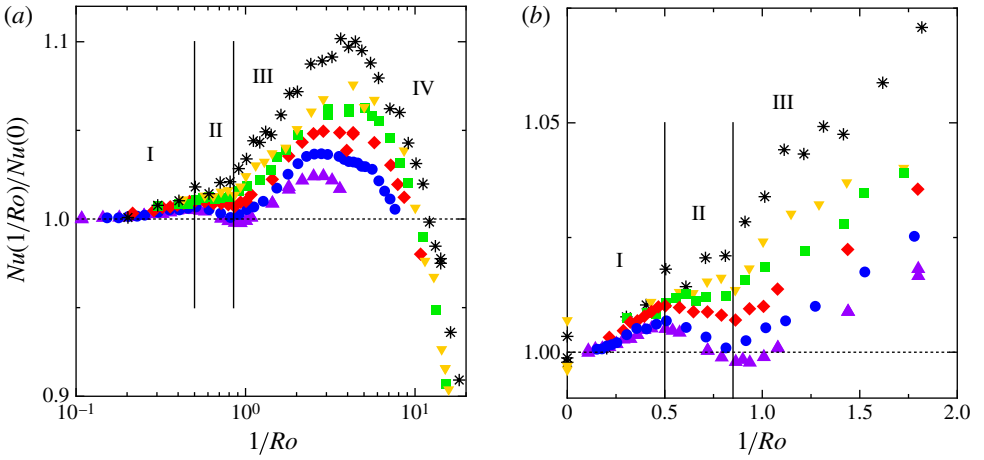

FIGURE 1. (Colour online available at journals.cambridge.org/flm) Reduced Nusselt number $Nu_{red} = Nu(1/Ro)/Nu(0)$ as a function of $1/Ro$ for $Ra = 2.3 \times 10^9$ (run E12, stars, black online), $Ra = 4.5 \times 10^9$ (run E13, down-pointing triangles, yellow online), $Ra = 9.0 \times 10^9$ (run E14, squares, green online), $Ra = 1.80 \times 10^{10}$ (run E15, diamonds, red online), $Ra = 3.59 \times 10^{10}$ (run E16, bullets, blue online) and $Ra = 7.2 \times 10^{10}$ (run E17, up-pointing triangles, purple online). In (*a*) data are shown over a large $1/Ro$ range with a logarithmic horizontal scale. In (*b*) data are shown for $1/Ro < 2.0$ on a linear scale. The vertical solid lines indicate the bifurcations at $1/Ro_0$ and $1/Ro_c$. The roman numbers in the figures correspond to the regions discussed in the text. Figure adapted from figure 2 of Weiss & Ahlers (2011*a*).

The existence of a maximum of Nu, and the negative slope of $Nu(1/Ro)$ in range IV beyond it, can be attributed to two phenomena. On the one hand, it is known that for large $1/Ro$ vertical fluid motion (and, thus, heat transport) is suppressed due to the Taylor–Proudman effect (see, for instance, Tritton 1988). On the other hand, it is expected that the heat-transport enhancement is maximal when the Ekman BL δ_E has a thickness that is similar to that of the thermal BL δ_θ. Since the Ekman layer shrinks with increasing rotation rate ($\delta_E \propto Ek^{1/2}$) its thickness becomes smaller than δ_θ at a certain $1/Ro$ and then the Ekman vortices no longer are able to effectively pump fluid out of the thermal BL into the bulk region (Julien *et al.* 1996; King *et al.* 2009; Liu & Ecke 2009; Stevens, Clercx & Lohse 2010).

It is so far unknown to us why Nu increases slightly in range I and which mechanism can explain the slow decrease in range II. To compare the behaviour of $Nu(1/Ro)$ with the measurements of the temperature at the sidewall, we mark in the following figures, whenever useful, the critical inverse Rossby numbers $1/Ro_0 = 0.5$ (transition between ranges I and II) and $1/Ro_c = 0.85$ (transition between ranges II and III).

4. The temperature gradient at the sidewall

In turbulent thermal convection the vertical temperature gradient in the thermal BLs at the top and bottom plates is very large, while in the bulk region the gradient is relatively small (see, e.g., Tilgner, Belmonte & Libchaber 1993; Du & Tong 2000; Brown & Ahlers 2007). The local vertical temperature gradient in the bulk is not constant over the entire horizontal cross section. It is relatively larger at the sidewall where the plumes travel primarily, and smaller in the centre (close to the axis of

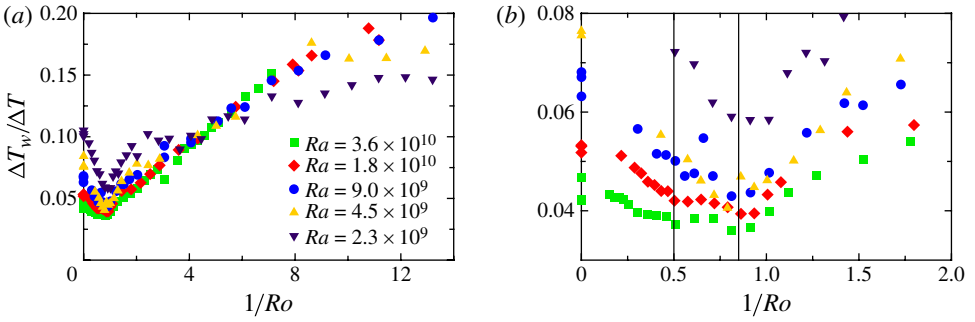

FIGURE 2. (Colour online) Reduced temperature gradient along the sidewall $\Delta T_w/\Delta T$ for $Ra = 2.3 \times 10^9$ (run E12, stars, black online), $Ra = 4.5 \times 10^9$ (run E13, triangles, yellow online), $Ra = 9.0 \times 10^9$ (run E14, squares, green online), $Ra = 1.80 \times 10^{10}$ (run E15, diamonds, red online) and $Ra = 3.59 \times 10^{10}$ (run E16, bullets, blue online). (*a*) Large range. (*b*) Only $1/Ro < 2$. The up-pointing triangles show data for $Ra = 7.17 \times 10^{10}$ (run E17). The vertical solid lines indicate the bifurcations at $1/Ro_0$ and $1/Ro_c$.

the cylindrical convection vessel) where there are very few plumes. For sufficiently small Ra, and Pr near five, a small negative (stabilizing) gradient was measured at the cylinder axis (Tilgner *et al.* 1993; Brown & Ahlers 2007).

We define the relative gradient along the wall as

$$\Delta T_w/\Delta T = [2 \cdot (\langle T_{i,b}\rangle - \langle T_{i,t}\rangle)]/\Delta T, \tag{4.1}$$

where the average is taken over all eight thermistors and all times (after transients have decayed) during a single experimental run. For a cylindrical sample with $\Gamma = 1$ it was shown by Brown & Ahlers (2007) that an increase of Ra leads to smaller relative gradients at the sidewall but also to smaller negative relative gradients at the cylinder axis. For $\Gamma = 0.50$, measurements of the sidewall temperature gradient as a function of the Rayleigh number were obtained recently by Weiss & Ahlers (2011*b*) using the present apparatus without rotation. The results, as a function of Ra, overlap somewhat with and follow nearly the same power law as the data for $\Gamma = 1$ (Brown & Ahlers 2007), suggesting that the aspect ratio has only a minor effect in the non-rotating case.

Figure 2 shows new data for the relative temperature gradient along the sidewall in the presence of rotation for $\Gamma = 0.50$, $Pr = 4.38$ and several Ra as a function of $1/Ro$. As can be seen in figure 2(*a*), $\Delta T_w/\Delta T$ decreases with increasing $1/Ro$ for small rotation rates ($1/Ro \lesssim 1/Ro_c$) and increases for larger rotation rates ($1/Ro \gtrsim 1/Ro_c$). The increase can be attributed to an enhanced lateral mixing in the presence of rotation as explained by Julien *et al.* (1996). This lateral mixing reduces the temperature contrast and thus the buoyancy, resulting in a reduced vertical fluid motion and reduced vertical heat transport. At very fast rotation rates Stewartson layers form at the sidewalls (Kunnen *et al.* 2011) in which additional warm (cold) fluid is pumped from the bottom (top) plate in the vertical direction. Therefore our top and bottom sets of probes are not in direct contact with the bulk flow, but are influenced by these BLs. As a result the temperature gradient at the sidewall is expected to be slightly larger than in the bulk. The flow velocity in the Stewartson layers is in general small and influences mainly the sidewall regions close to the top and bottom boundaries (as shown for example in figure 6 of Kunnen *et al.* 2011). Therefore we believe that, especially in the $\Gamma = 0.50$ case, these layers have only a minor influence on our sidewall temperature measurements.

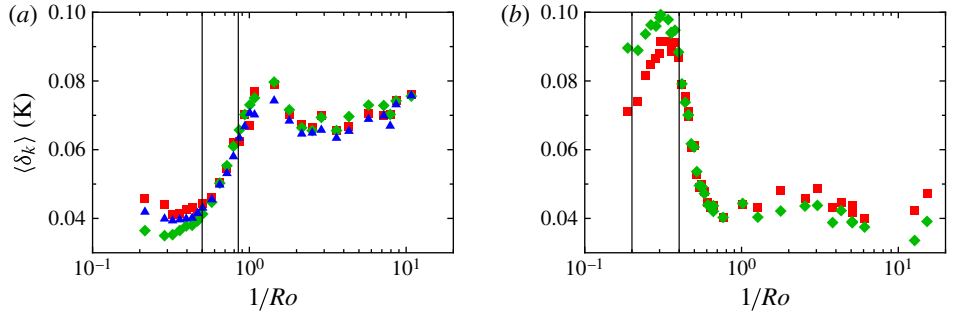

FIGURE 3. (Colour online) (*a*) The time-averaged LSC amplitudes δ_k for all three levels $k = b$ (squares, red online), m (diamonds, green online) and t (triangles, blue online) as a function of $1/Ro$ for $\Gamma = 0.50$ and $Ra = 1.80 \times 10^{10}$ (run E15). (*b*) The same quantity as in (*a*) but for $\Gamma = 1.00$ and $Ra = 2.25 \times 10^{9}$ (run E6 of Zhong & Ahlers 2010). Here data were only available for $k = b$ and m. The black vertical lines mark $1/Ro_0$ and $1/Ro_c$. For both (*a*) and (*b*) the applied temperature difference was $\Delta T = 3.98$ K.

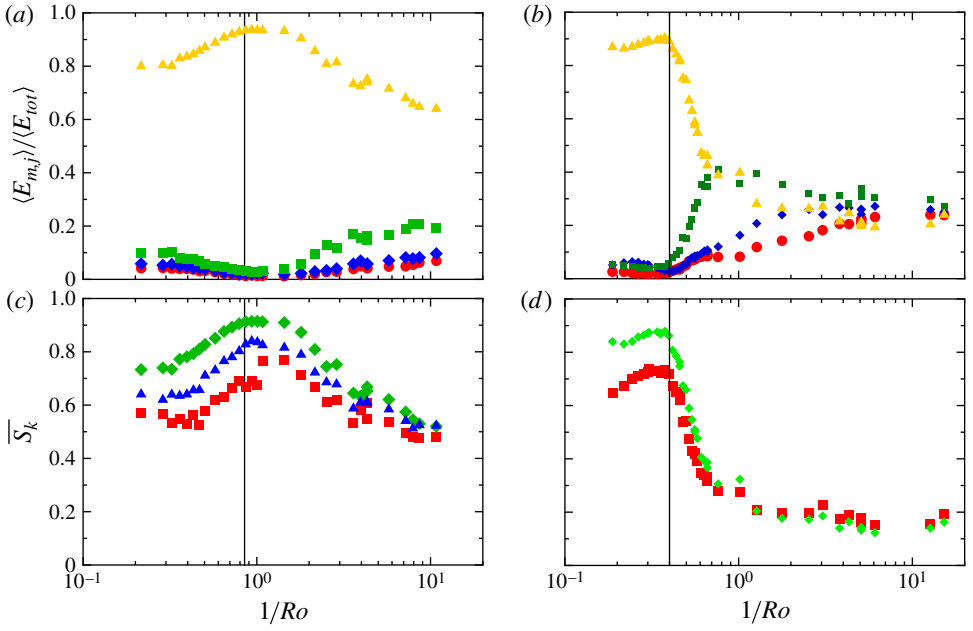

FIGURE 4. (Colour online) (*a*) The time-averaged energies $\langle E_{m,j} \rangle / \langle E_{tot} \rangle$ of the Fourier modes $j = 1, \ldots, 4$ for data from the middle thermistor row of the present sample with $\Gamma = 0.50$ for $Ra = 1.80 \times 10^{10}$ (run E15). Triangles (yellow online): $j = 1$. Squares (green online): $j = 2$. Diamonds (blue online): $j = 3$. Circles (red online): $j = 4$. (b) The same as (*a*), but for $\Gamma = 1.0$ and $Ra = 2.25 \times 10^{9}$ (run E6 of Zhong & Ahlers 2010). (*c*) The LSC strength $\bar{S}_k$ for all three levels $k = b$ (squares, red online), m (diamonds, green online) and t (triangles, blue online) of the same run as in (*a*). (*d*) Same as (*c*), but for the data used to generate (*b*) (in this case data were available only for $k = b$ and m).

The origin of the decrease of ΔT_w for small $1/Ro$ is not known to us. It was observed as well for $\Gamma = 1$ (Zhong & Ahlers 2010). However, we note that for both Γ the thermal amplitude δ_m (figure 3), and thus the energy of the lowest Fourier mode $E_{m,1}$, of the LSC increases in the same range of $1/Ro$, see figure 4 below and figure 21

of Zhong & Ahlers (2010). Thus, it appears that a more vigorous LSC reduced the sidewall thermal gradient. It will be interesting to extend the model of Brown & Ahlers (2008*b*) by including the Coriolis force in order to see whether this leads to an increase of δ_m and $E_{m,1}$. Such an extension should be possible at least for $\Gamma = 1$ over the $1/Ro$ range below $1/Ro_c$ where Ekman vortices are not yet adding further complications.

For $Ra = 10^9$ and $Pr = 6.4$ the gradient in the sample interior along the vertical centre line of a $\Gamma = 1$ sample was studied using DNS by Zhong *et al.* (2009) and Kunnen, Geurts & Clercx (2010). For small rotation rates a significant stabilizing gradient was found to develop; but for $1/Ro \gtrsim 0.3$ a strong destabilizing gradient evolved with increasing $1/Ro$. Thus, it seems safe to conclude that, at large $1/Ro$, the destabilizing gradient observed by us along the sidewall is a bulk effect and not just confined to the vicinity of the walls.

5. The LSC under the influence of rotation

5.1. *The strength of the LSC*

Figure 3(*a*) shows $\langle\delta_k\rangle$, i.e. the time-averaged amplitude of the sinusoidal temperature modulation, as defined by (2.1), for the top, middle and bottom thermistor row. At very low rotation rates, $\langle\delta_m\rangle$ is smaller than $\langle\delta_t\rangle$ and $\langle\delta_b\rangle$. This is in agreement with previous measurements for the non-rotating case (Weiss & Ahlers 2011*b*). Part of the reason for the lower $\langle\delta_m\rangle$ is the existence of the DRS. During the time when the system is in the DRS, δ_m is very small. This leads to a smaller $\langle\delta_m\rangle$. We show in § 5.3 that for small $1/Ro$ the fraction of time w(DRS) that the system spends in the DRS becomes smaller as $1/Ro$ increases and essentially vanishes near $1/Ro_0$. However, even at the smallest $1/Ro$, where w(DRS) is largest, it is only about 0.08; and from figure 3(*a*) we see that $\langle\delta_m\rangle$ is smaller than $\langle\delta_b\rangle$ or $\langle\delta_t\rangle$ by two or three times that fraction. Thus, the presence of the DRS cannot be the entire reason for the relatively small $\langle\delta_m\rangle$.

For very small $1/Ro$ one sees that $\langle\delta_t\rangle < \langle\delta_b\rangle$. This is not expected, since there is no mechanism (known to us) that can break the up–down symmetry. Furthermore, a systematic measurement error can be excluded as well, since both for $1/Ro = 0$ and $1/Ro > 0.5$ all three $\langle\delta_k\rangle$ coincide with each other. One can speculate that slightly more half-turns (see § 5.7) occur in the bottom part of the cell than in the top part, which is not obvious from figure 19. Note, however, that similar asymmetries between the top and bottom part of the cell are also observed in other quantities of the LSC (see, for instance, figure 4).

For $1/Ro > 1/Ro_0$ all $\langle\delta_k\rangle$ are of equal size and increase with increasing $1/Ro$ until they reach a maximum near $1/Ro \approx 1.5$. From there on $\langle\delta_k\rangle$ decreases slightly and then, for $1/Ro > 3$, increases again very slightly. In general, the amplitudes stay at a level that is significantly higher than it is without rotation.

To compare with similar experiments in cylinders with aspect ratio $\Gamma = 1.00$, we plot $\langle\delta_b\rangle$ and $\langle\delta_m\rangle$ of dataset E6 from Zhong & Ahlers (2010) in figure 3(*b*). In contrast to the $\Gamma = 0.50$ measurements, one sees that for $\Gamma = 1.00$ and very small rotation rates the amplitude at the middle thermistor row is significantly larger than that at the bottom thermistor row. One can argue that this is due to the shape of the LSC, which for $\Gamma = 1.00$ is roughly circular (Xi & Xia 2008*b*) and thus more effective in cooling or heating the sidewall at the midplane; but it is difficult to quantify this idea. One sees that $\langle\delta_k\rangle$ increases with increasing $1/Ro$ also for $\Gamma = 1.00$. It reaches a maximum at $1/Ro \approx 0.3$. In contrast to the $\Gamma = 0.50$ case, the location of

this maximum is well below $1/Ro_c$. For larger $1/Ro\langle\delta_k\rangle$ decreases and finally stays at a rather low constant level significantly smaller than without rotation.

For large $1/Ro$ it is important to note that the temperature amplitudes $\langle\delta_k\rangle$ most likely do not represent the strength of the LSC. For $1/Ro > 1/Ro_c$ vortices occur first close to the top and bottom boundaries, but increase in length so that they reach also into the bulk region as $1/Ro$ increases. As a result the flow structure, and the azimuthal temperature variation at the sidewall, is expected to become more and more dominated by vertical vortices that destroy the LSC signature of the flow (Stevens *et al.* 2011*a*).

5.2. *The existence range of the LSC*

From the fit of (2.1) to the eight $T_{i,k}$, and the resulting $\langle\delta_k\rangle$ shown above in § 5.1, it is difficult to determine whether only the strength of the LSC changes or whether the LSC structure changes or disappears. In an attempt to illuminate this problem, we carried out the complete Fourier analysis suggested by Stevens *et al.* (2011*a*) and outlined in § 2.2. Figure 4(*a*) shows the time-averaged energies of the four accessible Fourier modes as a function of $1/Ro$ for our $\Gamma = 0.50$ and $Ra = 1.8 \times 10^{10}$. Keeping in mind that $E_{k,1} = \delta_k^2$, we do not expect new insight from the results for the energy $\langle E_{k,1}\rangle/\langle E_{tot}\rangle$ of the first Fourier mode. The new information is that, over the whole range $0 \leqslant 1/Ro \leqslant 12$, $\langle E_{k,1}\rangle$ was significantly larger than the energies of all of the higher modes. This could be interpreted to imply that a well-defined LSC existed at least up to $1/Ro = 12$. However, as discussed later in this section, this evidence may be illusory.

As was seen for $\langle\delta_k\rangle$, $\langle E_{k,1}\rangle/\langle E_{tot}\rangle$ increased and reached a maximum quite close to $1/Ro_c$. This maximum was located just above (below) $1/Ro_c$ for $\Gamma = 0.5$ ($\Gamma = 1.00$). This result stands in contrast to the DNS results of Kunnen *et al.* (2011) for $\Gamma = 1$ which showed a monotonically decreasing $\langle E_{m,1}\rangle/\langle E_{tot}\rangle$. However, Kunnen *et al.* (2011) used numerical probes that were located inside the sample at a distance of $0.05D$ away from the sidewall. We do not know whether this difference in probe location is responsible for the different results, but it seems unlikely to us. The increase of $\langle E_{k,1}\rangle$ observed in the experiments corresponds to a stabilization of the SRS of the LSC by the rotation, as we discuss further in § 5.3.

The LSC strengths $\bar{S}_k$ for the top ($\bar{S}_t$), middle ($\bar{S}_m$) and bottom ($\bar{S}_b$) thermistor rows are shown in figure 4(*c*). Of course the $\bar{S}_k$ curves look very similar to those for $\langle E_{k,1}\rangle/\langle E_{tot}\rangle$. As expected, all three $\bar{S}_k$ show qualitatively the same behaviour. At a quantitative level $\bar{S}_m$ is larger than the other two. This behaviour can be explained by the larger number of events at the bottom or top (see § 5.5) that are in part due to half-turns, where a section of the single LSC roll becomes decoupled from the rest (see § 5.7). Therefore, one often still has an LSC temperature signature in the middle, while it is already destroyed at the top or bottom. More surprisingly, $\bar{S}_b < \bar{S}_t$ for small $1/Ro$, showing that there is an asymmetry between top and bottom. We do not have an explanation for this result. An inaccurate temperature measurement can be excluded since all $\bar{S}_k$ become very close for larger $1/Ro$ and also for $1/Ro = 0$ (not shown in figure 5, but see figure 19 of Weiss & Ahlers 2011*b*). For very large rotation rates, the symmetry is expected to be broken, since warm fluid is pushed inwards due to centrifugal forces while cold fluid is pushed outward. However, even for the largest rotation rates in our experiments, the Froude number that measures the ratio between centrifugal forces and buoyancy is $Fr = \Omega D^2/4g \approx 0.01$, suggesting that centrifugal forces do not play a significant role. Similar asymmetries between the top and bottom

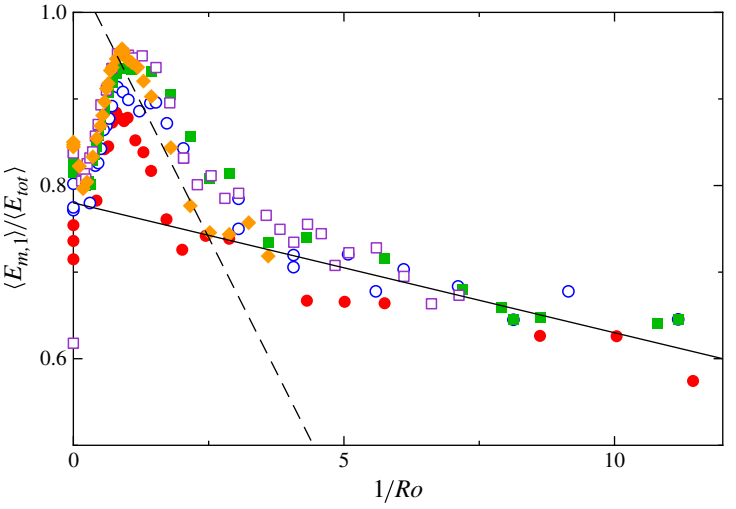

FIGURE 5. (Colour online) The time-averaged energies $\langle E_{m,1}\rangle/\langle E_{tot}\rangle$ of the fundamental Fourier mode for data from the middle thermistor row of the present sample with $\Gamma = 0.50$ for $Ra = 4.51 \times 10^9$ (solid circles, red online, run 13), 9.0×10^9 (open circles, blue online, run E14), 1.80×10^{10} (solid squares, green online, run E15), 3.59×10^{10} (open squares, purple online, run E16) and 7.17×10^{10} (solid diamonds, orange online, run E17). The dashed (solid) line has a slope of -0.124 (-0.015).

thermistor rows were observed also in other quantities, such as the event rate (§ 5.5) or the instantaneous rotation rates $\Delta\theta/\Delta t$ (figure 9).

The differences between the $\bar{S}_k$ become smaller with increasing $1/Ro$. This is similar to the differences between the rates of events (see figure 12 below).

For comparison, the right-hand side of figure 4 (4*b* and 4*d*) shows similar results for $\Gamma = 1$. In this case, after the initial increase $\langle E_{m,1}\rangle$ decreased rapidly beyond its maximum while the other modes, especially $j = 2$, had increasing energies. At $1/Ro \approx 0.8, j = 1$ was no longer the dominant mode since its energy $\langle E_{m,1}\rangle$ fell below $\langle E_{m,2}\rangle$, and thus we assume that the LSC had ceased to exist. Correspondingly, also $\bar{S}_m$ and $\bar{S}_b$ in figure 4(*d*) showed a slight increase for small $1/Ro$, and then a steep decrease after their maxima at $1/Ro_c$. The conclusions drawn here regarding the survival of the LSC for $\Gamma = 1$ are consistent with those based on comparing $\langle\delta_k\rangle$ with $\langle\sigma_{f,k}\rangle$ (see (2.2)) as was done by Zhong & Ahlers (2010).

It is surprising and unexpected that, for $\Gamma = 0.50$, the LSC appears to exist even for $1/Ro = O(10)$ (see figure 4*a*). In this range, the formation of vortices that extend through the whole cell is expected to take place (Kunnen 2008; Stevens *et al.* 2011*b*). A deeper insight into the real flow structure is experimentally not accessible to us. However, DNS of the Boussinesq equations have revealed that, also for $\Gamma = 0.50$, vortex columns extend over almost the whole cell height for $1/Ro \gtrsim 3$. As shown in figure 5 of Stevens *et al.* (2011*b*), for $1/Ro = 3.33$ and $Ra = 2.91 \times 10^8$, only two vortices exist for this small aspect ratio. One of them originates at the bottom and extracts warm fluid out of the bottom BL, while a similar one originates at the top and extracts cold fluid out of the top BL. Both are located next to each other roughly on a sample diameter, and one can expect that this flow configuration would show a sinusoidal azimuthal temperature signature at the sidewall, similar to that we find when an LSC is present. Thus, this two-vortex structure could not be distinguished from

an LSC by the methods used in our experiment. However, figure 5 of Stevens *et al.* (2011*b*) shows only one snapshot and it is not known whether this flow configuration with only two counter-rotating vortices will persist in time and as a function of Ra and $1/Ro$. In further discussions we shall refer to this state as the two-vortex state (TVS). If indeed it exists over a wide Ra and $1/Ro$ range, then our sidewall measurements, intended to shed light on the LSC dynamics, actually yield information about the TVS dynamics.

Searching for more evidence for the existence of the TVS, we examined in figure 5 the dependence of $\langle E_{m,1}\rangle$ on $1/Ro$ over a wide range and for all of the Ra values for which we had precise data. No significant dependence on Ra was revealed. One sees that immediately following the maximum there was a steep drop of $\langle E_{m,1}\rangle$ which we assume was associated with a diminishing strength of the LSC due to the interactions with Ekman vortices. Beyond $1/Ro \simeq 3$ the rate of decrease of $\langle E_{m,1}\rangle$ with $1/Ro$ was smaller by an order of magnitude, as indicated by a comparison of the slopes of the dashed and the solid line in the figure. It is not unreasonable to conjecture that the slower decrease of $\langle E_{m,1}\rangle$ is a characteristic of the TVS. We return to other characteristics possibly associated with the TVS in the next section.

5.3. *Flow-mode transitions*

Flow-mode transitions from a SRS to a DRS where two counter-rotating rolls are placed on top of each other were first found in experiments by Xi & Xia (2008*b*). Recently Weiss & Ahlers (2011*b*) reported in detail on the mechanism and statistics of flow-mode transitions of this kind for containers with aspect ratio $\Gamma = 0.50$. They showed that the fraction of time that the system spent in the DRS decreased with increasing Ra. Here we report on the influence of slow rotation on the lifetime and prevalence of the SRS and the DRS.

To identify these states, we used the same algorithm that was used by Weiss & Ahlers (2011*b*). We assumed that the system was in the DRS when $|\theta_t - \theta_b| > 120°$ and that the system was in the SRS when none of $|\theta_{k1} - \theta_{k2}|$ exceeded 60° for $k_1 \neq k_2$. In order to omit states where θ_k was poorly defined, we introduced an additional condition that took the δ_k into consideration. For a DRS δ_t and δ_b both had to be larger than 15 % of their average values, whereas to consider a state as a SRS all δ_k had to be larger than 15 % of their average values.

The fraction of time that the system spent in the SRS (w(SRS)) or the DRS (w(DRS)) is plotted in figure 6(*a*). The data show that w(SRS) increased from 0.67 for the non-rotating case up to 0.98 for $1/Ro \approx 1.2$. On the other hand, w(DRS) decreased from about 0.07 for the non-rotating case to zero for $1/Ro \approx 1.2$. The fraction of time $w_{other} = 1 - w(\mathrm{SRS}) - w(\mathrm{DRS})$ that the system spent in other states not meeting our SRS or DRS criteria, for instance in transients between states, is shown as black stars in the figure. It decreased from 0.26 to near zero over this $1/Ro$ range. Note, that the absence of any DRS means that no such flow mode was observed during a run of 24 h duration. For larger $1/Ro$ the SRS became less stable, as indicated by the decrease of w(SRS) and the increase of w(DRS).

A similar behaviour could be found by looking at the average time that the system spent either in the SRS or in the DRS. This is shown in figure 6(*b*). While the SRS was destroyed regularly in the non-rotating case (the average life time was about $7 \times 10^{-4}\tau_\kappa$) this state became more and more stable as the rotation rate increased. At $1/Ro = 1.4$, the average life time $\tau_{SRS} = 8 \times 10^{-3}$, a factor of 10 larger than in the non-rotating case. The DRS on the other hand became increasingly unstable and its lifetime was strongly reduced as $1/Ro$ got closer to one.

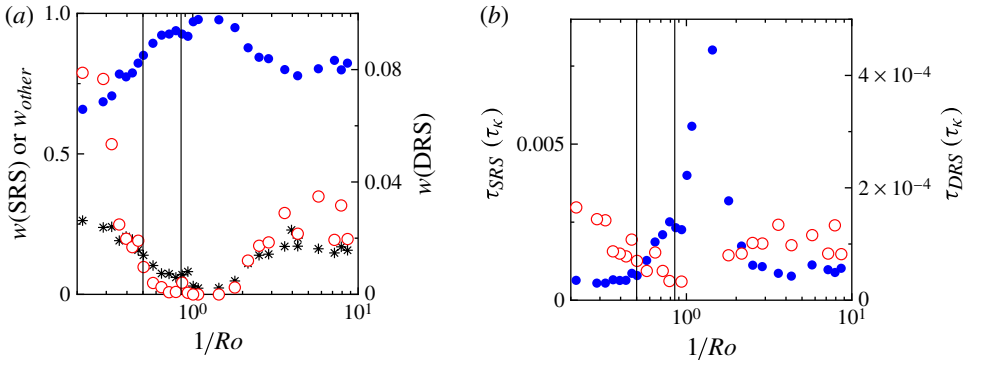

FIGURE 6. (Colour online) (*a*) The fractions of time w when the SRS, the DRS or some other state existed and (*b*) the lifetimes (in units of the vertical thermal diffusion time τ_κ) of the SRS and the DRS, both as a function of $1/Ro$ on a semilogarithmic scale. w(SRS): bullets, blue online, left ordinate. w(DRS): open circles, red online, right ordinate. w_{other}: black stars, left ordinate. The solid vertical lines mark $1/Ro_0$ and $1/Ro_c$. The data were taken at $Ra = 1.80 \times 10^{10}$ (run E15).

If the LSC actually does not exist for, say, $1/Ro \gtrsim 2$ or so, then, as discussed above, our measurements of w really pertain to the TVS. The probability w(SRS) is then a measure of the fraction of time during which both vortices extend sufficiently far through the cell to produce a sinusoidal azimuthal profile at all three measurement levels.

We conclude that slow and moderate rotation stabilizes the SRS significantly. We can only speculate about the reason for this stabilization. If one assumes that many SRS–DRS transitions are induced by small rolls at the corner of the cell that grow in size and finally replace the original roll, one can think that this process is hindered by the half-turns (see § 5.7) that occur regularly and that do not allow small corner rolls to grow to a significant size. However, these are only speculations and not backed up by measurements so far.

5.4. *The dynamics of the LSC*

The fit parameters $\delta_k(t)$ and $\theta_k(t)$ (see (2.1)), as well as their various correlations, yield information about the time evolution of the strength, orientation and shape of the LSC. Similarly, the Fourier analysis discussed in § 2.2 yields in part equivalent and in part complementary information.

Figure 7 shows $\delta_t(t)$, $\delta_m(t)$ and $\delta_b(t)$ for $1/Ro = 0$ and for the moderately rotating case $1/Ro = 0.79$. As noted before (Xi & Xia 2008*a*; Weiss & Ahlers 2011*b*), for $1/Ro = 0$ all δ_k are very erratic and fluctuate much more than they do in the $\Gamma = 1$ case (see, e.g., Brown & Ahlers 2006*b*; Xi & Xia 2008*a*,*b*; Weiss & Ahlers 2011*b*). While for $\Gamma = 1$ rare very small values of δ_k are mostly due to cessations where all three δ_k come close to zero simultaneously, for $\Gamma = 0.50$ these events are due to a variety of processes including flow-mode transitions, half-turns (see below), etc. where perhaps only a single δ_k becomes small. The dashed horizontal lines in figure 7 mark $0.15\langle\delta_k\rangle$: the threshold we used to determine flow-mode transitions, half-turns and other events. As can be seen in figure 7(*b*), in the presence of modest rotation the fluctuations become less vigorous and the events, where δ_k drops below the threshold, become less frequent for all three thermistor heights.

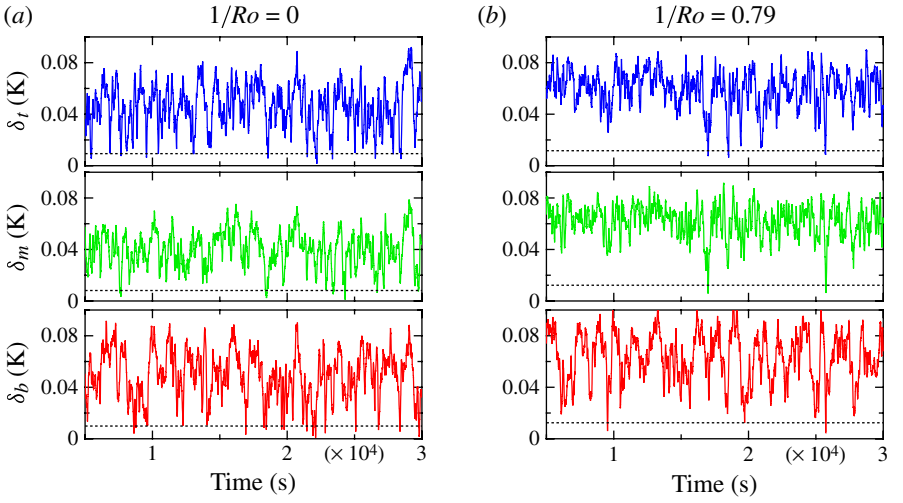

FIGURE 7. (Colour online) Examples of δ_t (top, blue online), δ_m (middle, green online) and δ_b (bottom, red online) as a function of time for $1/Ro = 0$ (left) and $1/Ro = 0.79$ (right) for $Ra = 1.8 \times 10^{10}$ (run E15). The dotted horizontal line in each graph gives the event threshold $0.15\langle\delta_k\rangle$.

Similar behaviour is observed also for the phases θ_k. However, for $1/Ro > 0$ the LSC rotates relative to the cylindrical container as was shown for $\Gamma = 1$ before by others (Hart *et al.* 2002; Kunnen *et al.* 2008; Zhong & Ahlers 2010) and is discussed in § 5.6 for $\Gamma = 0.50$. Therefore, we examine instead the phase differences between different thermistor rows $\theta_{k_1} - \theta_{k_2}$, which are not influenced by any net rotation, as a function of time. The results, given in figure 8, also show a stabilizing influence of slow rotation. For the non-rotating case (figure 8*a*), all curves most of the time have values close to multiples of 2π but fluctuate significantly around these values. These fluctuations are mostly random and are caused by the turbulent fluid flow, but also include contributions from the torsional mode (Funfschilling & Ahlers 2004; Funfschilling *et al.* 2008) of the LSC. In addition to these fluctuations, multiple 2π jumps occur that are mostly associated with SRS–DRS–SRS flow-mode transitions (see § 5.3) or other less well-defined events. Cessations are very rare for $\Gamma = 0.50$ (Weiss & Ahlers 2011*b*) and therefore make no significant contributions to these jumps. The 2π jumps occur when δ_k is small and consequently the uncertainty of θ_k is large. Thus, they may actually not have any real physical significance and instead may be due to the least-squares procedure used to fit the data as discussed in detail by Weiss & Ahlers (2011*b*, § 2.4).

When modest rotation is applied (figure 8*b*), the fluctuations around multiples of 2π are reduced, and there are not as many 2π jumps. The slow rotation apparently stabilizes the LSC, as noted already in § 5.2 where we examined the energy $E_{k,1}$ of the fundamental mode of the azimuthal temperature variation. We note that figures 7 and 8 are only examples for a specific $1/Ro$. As we show in § 5.5, close to $1/Ro = 1$ the event rate is minimal and therefore a single-roll LSC is most stable. This stability is reduced again for larger $1/Ro$.

A better picture of the effect of rotation on the dynamics and stability of the LSC is obtained from the corresponding probability distributions of δ_k and $\theta_{k_1} - \theta_{k_2}$. In both cases, we consider in detail three different rotation rates. These are the non-rotating

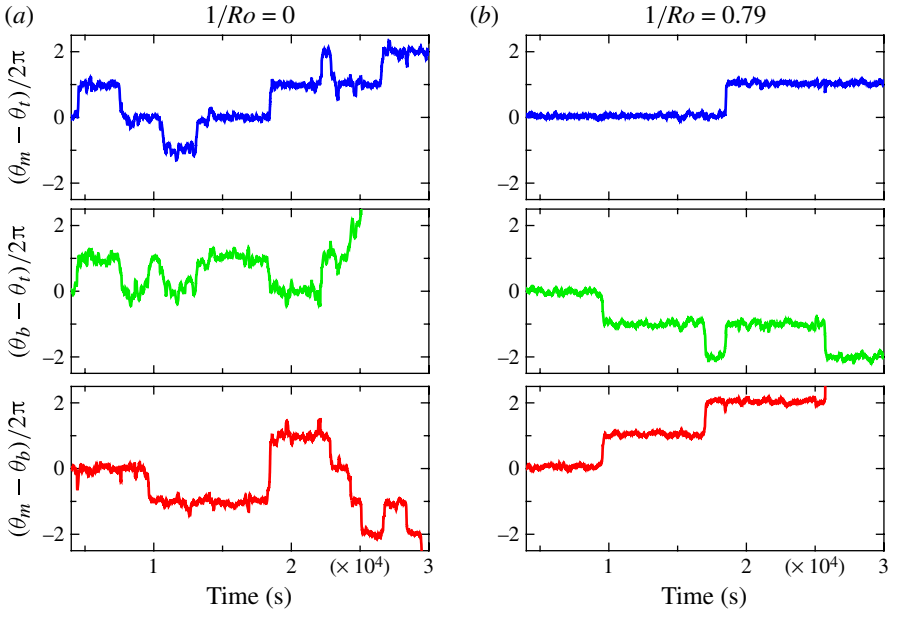

FIGURE 8. (Colour online) Example for $\theta_m - \theta_t$ (top panels, blue online), $\theta_b - \theta_t$ (middle panels, green online) and $\theta_m - \theta_b$ (bottom panels, red online) as a function of time for (*a*) $1/Ro = 0$ and (*b*) $1/Ro = 0.79$ and for $Ra = 1.8 \times 10^{10}$ (run E15).

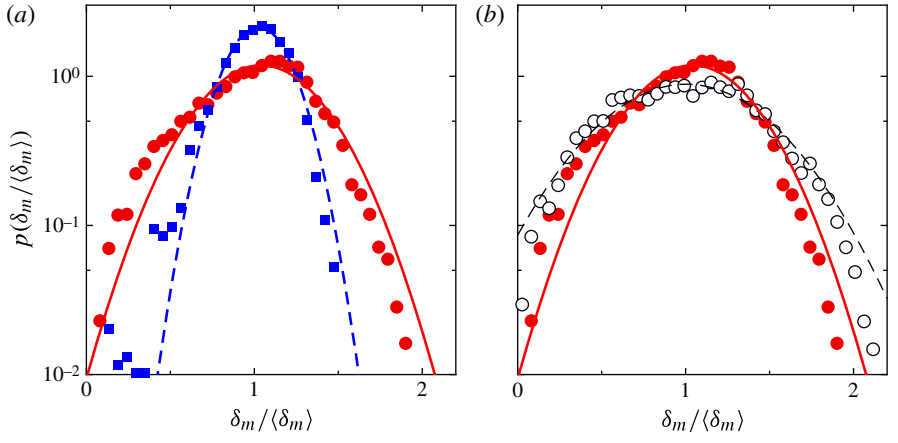

FIGURE 9. (Colour online) Comparison of the probability distributions of the normalized amplitude $\delta_m/\langle\delta_m\rangle$ for two values of $1/Ro > 0$ with the distribution for $1/Ro = 0$: (*a*) $1/Ro = 0.8$ (squares, blue online) and $1/Ro = 0$ (circles, red online); and (*b*) $1/Ro = 8.6$ (open circles, black) and $1/Ro = 0$ (solid circles, red online). The solid and dashed lines are Gaussian fits near the peaks. The Rayleigh number was $Ra = 1.8 \times 10^{10}$ (run E15).

case ($1/Ro = 0$), the case $1/Ro = 0.8$ which is just below the transition at $1/Ro_c$, and a very large rotation rate $1/Ro = 8.6$. Figure 9 shows $p(\delta_m/\langle\delta_m\rangle)$; but we noted that δ_t and δ_b behave similarly. Near their maxima the probability densities can be described quite well by a Gaussian function. For the non-rotating case ($1/Ro = 0$, solid circles, red online) the left tail is wider, while the right tail is slightly more narrow than a

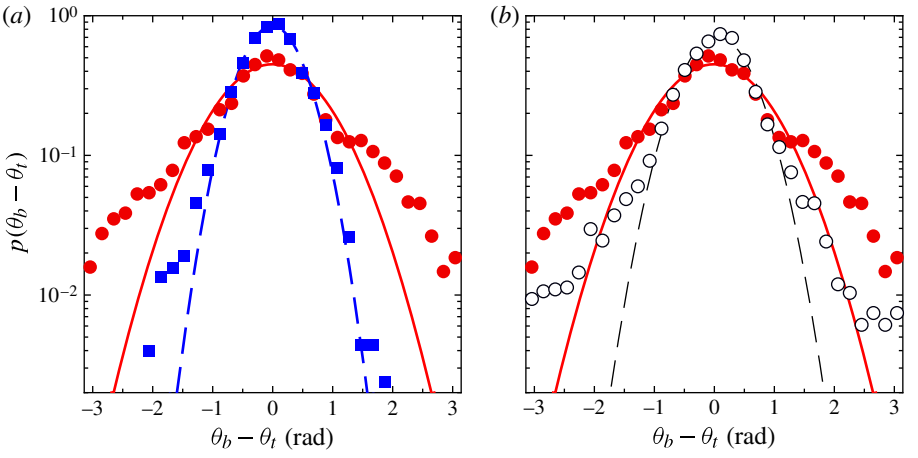

FIGURE 10. (Colour online) Comparison of the probability distributions of the phase difference between the top and the bottom $\theta_t - \theta_b$ for two values of $1/Ro > 0$ with the distribution for $1/Ro = 0$: (*a*) $1/Ro = 0.8$ (squares, blue online) and $1/Ro = 0$ (circles, red online); and (*b*) $1/Ro = 8.6$ (open circles, black) and $1/Ro = 0$ (solid circles, red online). The solid and dashed lines are Gaussian fits near the peaks. The Rayleigh number was $Ra = 1.8 \times 10^{10}$ (run E15).

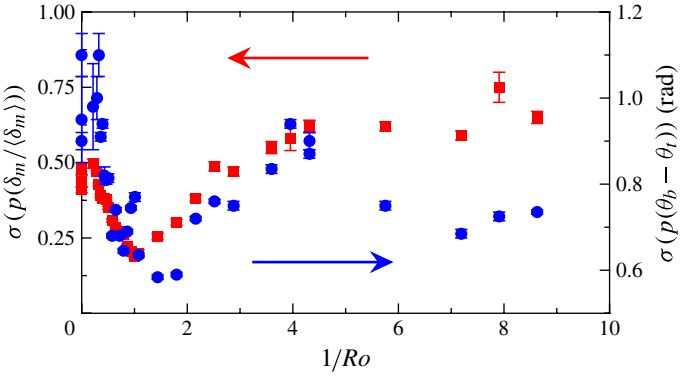

FIGURE 11. (Colour online) The width (square root of the variance) of the Gaussian fit to the probability density function of $\delta_m/\langle\delta_m\rangle$ as a function of $1/Ro$ (squares, red online, left ordinate) and the same quantity for the probability density function of $\theta_b - \theta_t$ (bullets, blue online, right ordinate). Data are from experiments with $Ra = 1.8 \times 10^{10}$ (run E15).

perfect Gaussian. From the data for $1/Ro = 0.8$ (figure 9*a*, solid squares, blue online) one sees that moderate rotation narrows the distribution significantly and brings the tails closer together. For the large rotation rate of $1/Ro = 8.6$ (figure 9*b*, open circles, black) the distribution becomes wider.

Figure 11 shows the widths of the Gaussian fits for different $1/Ro$ (squares, red online). Here, it becomes even more clear that the small rotation rates stabilize δ and narrow its probability density to a third of its width without rotation. A minimal width is reached at around $1/Ro = 1$, and for larger rotation rates the probability density becomes wider again.

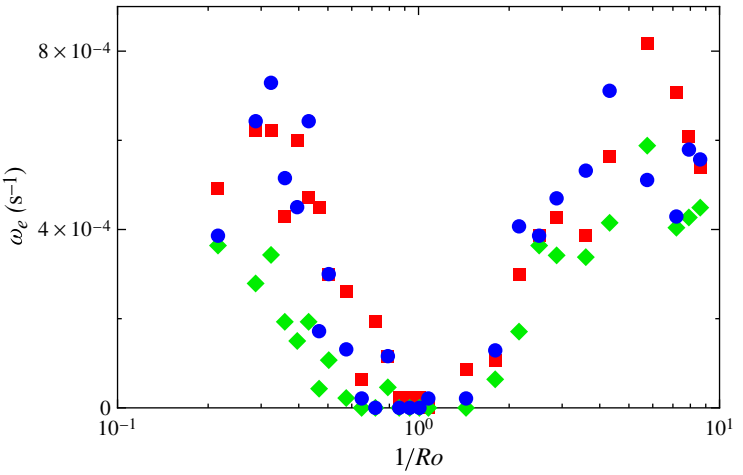

FIGURE 12. (Colour online) Frequency of events ω_e as a function of $1/Ro$ for the top (squares, blue online), middle (bullets, green online) and bottom (diamonds, red online) thermistor row for $Ra = 1.8 \times 10^{10}$ (run E15). The total measurement time for each data point was $\approx$4 to 5×10^4 s. Thus, the actual number of events was small and the uncertainty was large.

Very similar behaviour can also be seen in the probability distribution of $\theta_t - \theta_b$ as shown in figure 10. For the non-rotating case, a Gaussian function provides a good fit only near the maximum and the distribution has wide tails. These non-Gaussian tails likely are caused by the torsional oscillation which occurs when the system is in the SRS, as well as by regularly occurring flow-mode transitions to a DRS and back as described by Weiss & Ahlers (2011*b*). Small and moderate rotation (up to $1/Ro \simeq 1$) narrows not only the Gaussian part, but also brings the tails closer to the Gaussian distribution as seen in figure 10(*a*). This narrowing reflects the stabilization of the LSC and the suppression of flow-mode transitions by the rotation (see § 5.3). However, if one increases $1/Ro$ above $1/Ro \simeq 2$, the probability distribution becomes wider again but, in contrast to $p(\delta_m/\langle\delta_m\rangle)$, does not become as wide as it was for the non-rotating case. This is shown explicitly in figure 11 (bullets, blue online). The greater width for the larger $1/Ro$ must be regarded as a characteristic of the TVS if that state indeed prevails at these larger rotation rates.

In an effort to determine why the LSC is stabilized by modest rotation, we consider next the amplitudes δ_k as a function of time and determine how the number of events changes with $1/Ro$.

5.5. *Events*

A quick change of the orientation of the LSC is sometimes achieved by a cessation, a nearly complete breakdown of the LSC and its re-emergence after a short time period (Brown & Ahlers 2006*b*; Xi & Xia 2008*a*). In the past, to recognize cessations the amplitude of the LSC at the middle thermistor row δ_m was measured as a function of time. Usually an (arbitrary) threshold value $\delta_{th} = 0.15 \cdot \langle\delta_k\rangle$ (Brown & Ahlers 2006*b*; Xi & Xia 2008*a*; Weiss & Ahlers 2011*b*) was set and it was assumed that a cessation had occurred whenever δ_m had dropped below δ_{th}. This procedure was reliable for $\Gamma = 1.00$. However, for $\Gamma = 0.50$ it was found that flow-mode transitions to a DRS can also occur, with an associated drop of δ_m below δ_{th} while δ_b and/or δ_t remained

above the threshold (Xi & Xia 2008*b*; Weiss & Ahlers 2011*b*). In fact, it was found that, for $\Gamma = 0.50$ as well as $\Gamma = 1.00$, real cessations where all three amplitudes become small simultaneously are very rare and that, for $\Gamma = 0.50$, the much more frequent events, where only one or two amplitudes drop below the threshold, are associated with flow-mode transitions to a DRS or half-turns that will be introduced in § 5.7.

In the presence of rotation, Zhong & Ahlers (2010) showed for $\Gamma = 1.00$ that a moderate rotation rate increased the average number of events at midheight per unit time (ω_e) dramatically. The first strong increase by a whole order of magnitude occurred up to $1/Ro \approx 0.2$, which corresponds to $1/Ro_0$ for that Γ. A second increase appeared near their $1/Ro_c \approx 0.4$, where the event rate ω_e increased by another factor of three or so. A further increase of the rotation rate led to a further continuous increase of ω_e.

In the present case, for $\Gamma = 0.50$, the situation is different as can be seen in figure 12. Slow rotation decreased ω_e by nearly two orders of magnitude. A minimum rate was found near $1/Ro \approx 1$, and for larger rotation rates ω_e increased again. The statistical errors are fairly large and the exact location of the minimum is hard to determine. Thus, we are not able to establish any clear relationship between the location of the minimum and $1/Ro_0$ or $1/Ro_c$. We note that the rather large ω_e of about 5×10^{-4} s^{-1} (nearly two per hour) observed for $1/Ro \gtrsim 2$ would be a property of the TVS if that state indeed exists for our Ra.

We know of two $(1/Ro)$-dependent processes that influence ω_e for $\Gamma = 0.50$. Without rotation events are mainly due to flow-mode transitions. As was shown in § 5.3, slow rotation increases the stability of the LSC with respect to flow-mode transitions (see figure 6) and thus reduces ω_e. For $1/Ro > 1$ the SRS becomes less stable again and more flow-mode transitions to the DRS occur. The second process is discussed in § 5.7. There we show that, for slow rotation, the LSC rotates faster in the middle than it does near the top and bottom. This leads to partial destruction of the LSC (half-turns), resulting in an event rate that is larger than it is without rotation. The competition between these two phenomena will largely determine ω_e. The decrease of flow mode transitions with increasing $1/Ro$ initially has a larger effect than the increase of the frequency of half-turns, and thus the overall number of events has a minimum. This also explains, while for small $1/Ro$ ω_e for the middle thermistor row is significantly smaller than for the top and bottom.

5.6. *Rotation of the LSC*

In convection experiments with a slowly rotating container of aspect ratio $\Gamma = 1$ (Zhong & Ahlers 2010), the LSC was observed, in the frame of the rotating sample, to rotate with angular velocity $\omega < 0$, i.e. in the retrograde direction relative to the container rotation Ω. One can understand this observation qualitatively by considering the angular momentum of the LSC that tends to keep the orientation of the LSC plane constant in the inertial frame. Thus, if the LSC can be treated as a simple flywheel, then in the absence of dissipation its plane should rotate with $\omega = -\Omega$ in the rotating frame (Hart *et al.* 2002; Brown & Ahlers 2006*a*, 2008*a*). It was assumed that only the viscous friction at the sidewall 'pushes' the LSC to follow the container rotation and thus results in a smaller retrograde rotation ($0 > \omega > -\Omega$).

Initially we used the same analysis as that used by Zhong & Ahlers (2010) for $\Gamma = 1$ to calculate the rotation rate of the LSC for $\Gamma = 0.50$. That included first a fit of (2.1) to the thermistors in each row for each time step. A straight-line fit was then

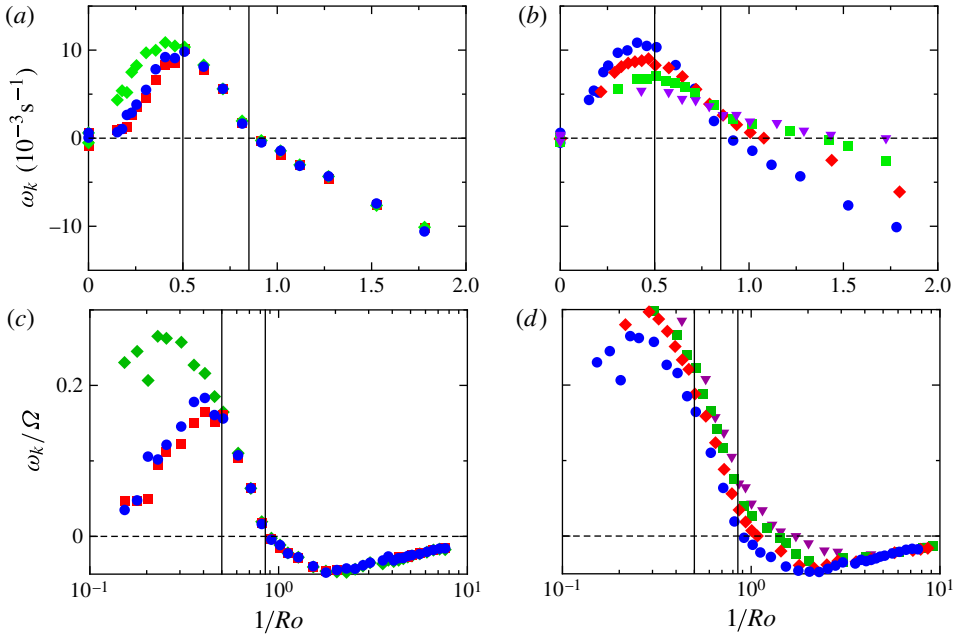

FIGURE 13. (Colour online) The average rotation rate $\omega_k = \langle \mathrm{d}\theta_k/\mathrm{d}t \rangle$ of the LSC. (*a*) Rotation rates for $Ra = 3.59 \times 10^{10}$ (run E16) for the three thermistor rows at the top (bullets, blue online), the middle (diamonds, green online) and the bottom (squares, red online). (*b*) The rotation rate $\omega_m = \langle \mathrm{d}\theta_m/\mathrm{d}t \rangle$ for the middle thermistor row for $Ra = 4.5 \times 10^9$ (triangles, purple online, run E13), $Ra = 9.0 \times 10^9$ (squares, green online, run E14), $Ra = 1.80 \times 10^{10}$ (diamonds, red online, run E15) and $Ra = 3.59 \times 10^{10}$ (circles, blue online, run E16). (*c*) and (*d*) show the same data as (*a*) and (*b*) but normalized by the rotation rate Ω of the cylinder. The vertical lines show $1/Ro_0$ and $1/Ro_c$. The dashed horizontal lines mark $\omega_k = 0$.

done to all $\theta_k(t)$ in order to determine

$$\omega_k = \left\langle \frac{\mathrm{d}\theta_k}{\mathrm{d}t} \right\rangle_t \tag{5.1}$$

for each k. The results, shown in figure 13, are surprisingly different from the results for $\Gamma = 1$. For small $1/Ro$, prograde rotation (i.e. $\omega_k > 0$) was observed, i.e. the LSC rotated in the same direction as and faster than the container. The rotation rate reached a maximum close to $1/Ro_0$ and decreased for larger $1/Ro$. For $1/Ro \approx 1$ (the exact value depends on Ra), all three ω_k reached zero and became negative for larger rotation rates. Thus, for these large Ω a retrograde rotation existed, albeit with $-\omega/\Omega \ll 1$.

By comparing ω_m for different Ra (figure 13*b*), one observes in the region of prograde rotation that ω_m is larger for the larger Ra. Near $1/Ro_0$, where ω_m has a maximum, the Ra dependence is strongest, while close to the second transition at $1/Ro_c$ ω_m is nearly independent of Ra. The dependence on Ra disappears when one normalizes ω_k by the container rotation rate Ω. As shown in figure 13(*d*), all curves ω_k/Ω behave very similarly. There is a slight decrease as Ra is increased which is more or less independent of $1/Ro$.

Another interesting phenomenon can be seen in figure 13(*a*), where ω_m is plotted for the top (circles, blue online), the middle (diamonds, green online) and the bottom

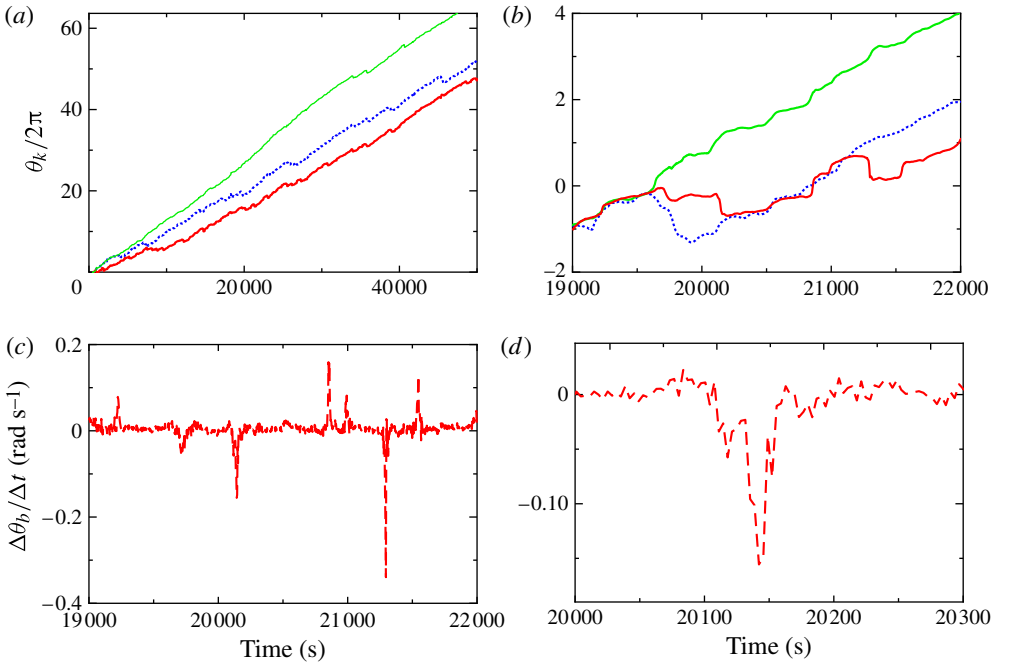

FIGURE 14. (Colour online) (*a*) Plots of θ_b (dashed, red online), θ_m (solid, green online) and θ_t (dotted, blue online) as a function of time for $Ra = 1.80 \times 10^{10}$ (run E15) and $1/Ro = 0.4$. (*b*) A short section of (*a*) with all points shifted vertically by multiples of 2π to make them collapse at 1.9×10^4 s. (*c*) The instantaneous rotation rate $\Delta\theta_b/\Delta t$ derived from the data for θ_b in (*b*). (*d*) An enlarged view of $\Delta\theta_b/\Delta t$ near the 2π jump of θ_b close to $t = 20\,140$ s. Plots of θ_k for larger $1/Ro$ are shown in the supplementary material (available at journals.cambridge.org/flm).

(squares, red online) thermistor row. While the top and bottom show nearly the same rotation rate, the middle one shows a significantly higher rotation rate for $1/Ro < 1/Ro_0$. This difference between ω_m on the one hand and $\omega_{b,t}$ on the other hand is even more pronounced for the normalized rotation frequency ω_k/Ω (figure 13*c*). For $1/Ro > 1/Ro_0$ the discrepancy between the ω_k at different heights disappears.

In order to find a possible reason for the difference between the rotation rates at the middle on the one hand and the top or bottom on the other hand we examined the time evolution of θ_k more closely in figure 14. The slopes of $\theta_k(t)$ are indeed different, but a closer look (figure 14*b*) shows that the difference seems to be caused at least in part by jumps of integer multiples of 2π that occur in θ_b and θ_t but not in θ_m.

We cannot tell whether the jumps are genuine rotations of the circulation plane because, when they occur, the corresponding amplitudes δ_k become small, the statistical errors of θ_k thus become large, and the jumps by 2π could be just a result of the least-squares fitting procedure (see Weiss & Ahlers 2011*b*, § 2.4). However, we do believe that at least in many cases the jumps are genuine and associated with a phenomenon to which we refer as half-turns and which is discussed in § 5.7. In any case, θ_m does not show many jumps and thus the prograde rotation seen there certainly is a genuine effect.

In order to avoid the influence of the jumps, particularly on ω_b and ω_t, we chose an alternative method of analysis. We used the phase difference $\Delta\theta_k$ between two

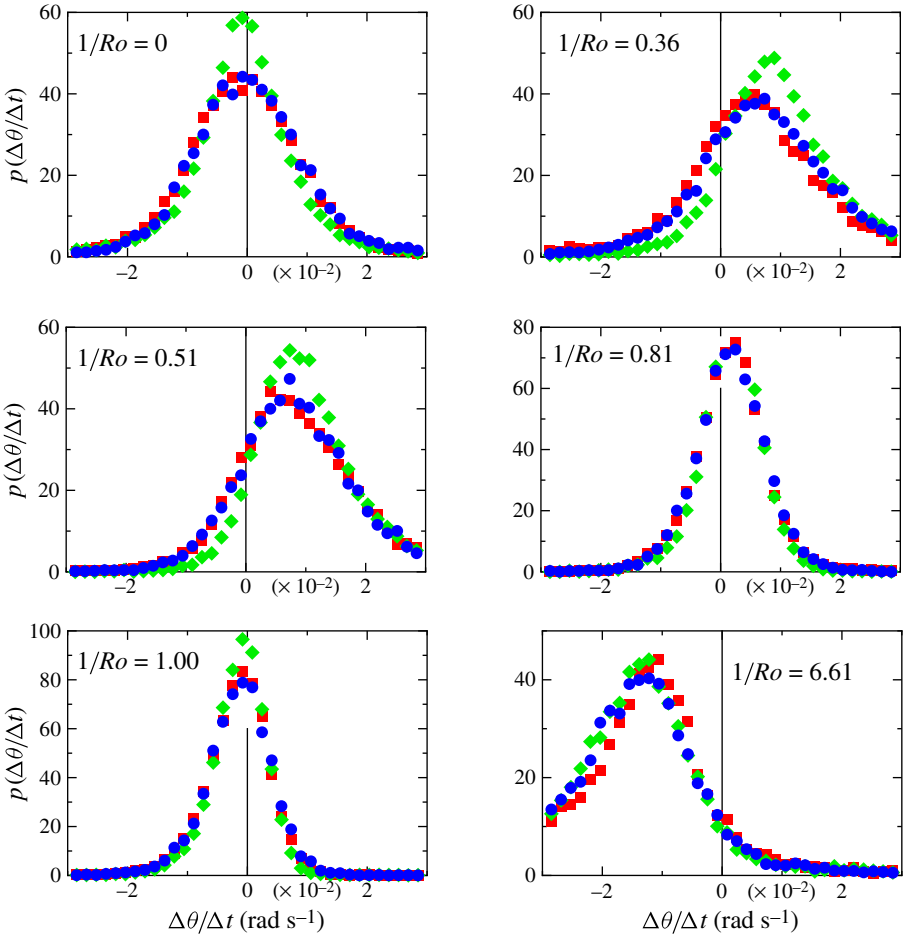

FIGURE 15. (Colour online) Probability distribution of $\Delta\theta_k/\Delta t$ for the top (bullets, blue online), the middle (diamonds, green online) and the bottom (squares, red online) thermistor row and for various $1/Ro$ (see legend). The Rayleigh number was $Ra = 3.6 \times 10^{10}$ (run E16).

successive time steps, separated typically by only a time increment of $\Delta t \simeq 3$ s, to calculate the near-instantaneous rotation rates $\dot{\theta}_k \equiv \Delta\theta_k/\Delta t$ and then determined the probability distribution $p(\dot{\theta}_k)$. An example of $\dot{\theta}_b$ is shown in figure 14(*c*), and with greater resolution in figure 14(*d*). There the 2π jumps appear as spikes along the time axis. During the jumps $|\dot{\theta}_k|$ is much larger than at other times; thus points during the jumps would fall onto the tails of the distribution and would not influence the locations of the maxima of $p(\dot{\theta}_k)$. Some results for $p(\dot{\theta}_k)$ are shown in figure 15.

Since the $p(\dot{\theta}_k)$ are nearly symmetric about their maxima, we can assume that the locations of the maxima give information about the average momentary rotation rate $\dot{\theta}_k$ of the LSC, excluding the jumps. One can see from figure 15 that the location of the maximum increases to positive values of $\dot{\theta}_k$ as $1/Ro$ increases from zero and remains positive up to $1/Ro \simeq 0.8 \simeq 1/Ro_c$, showing that prograde rotation prevails even when the jumps are excluded. For larger $1/Ro$ the maximum passes through zero near $1/Ro = 1.0$ and becomes negative, indicating retrograde rotation. This complex behaviour is shown more quantitatively in figure 16(*a*). There one can also see more

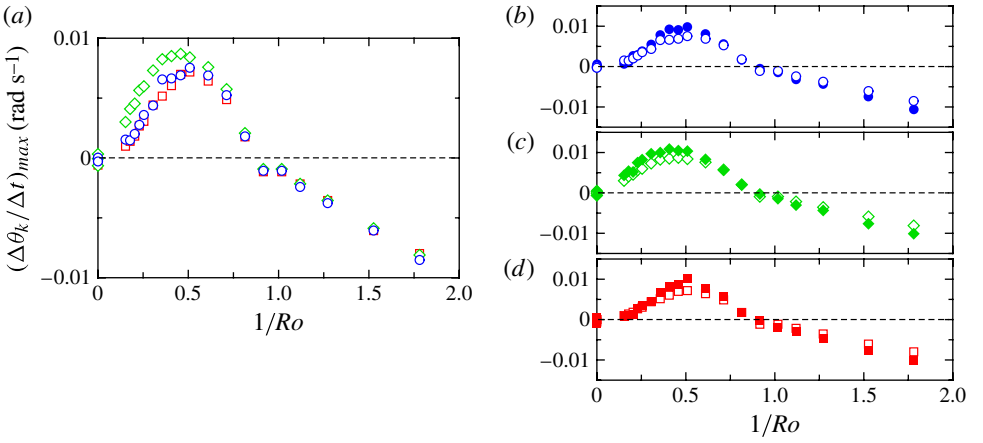

FIGURE 16. (Colour online) (*a*) The locations of the maxima of $p(\Delta\theta_k/\Delta t)$ as a function of $1/Ro$ for the bottom (open squares, red online), the middle (open diamonds, green online) and the top (open circles, blue online) thermistor rows. (*b–d*) Comparison of $\Delta\theta_k/\Delta t_{max}$ with the averaged rotation rate ω_k as shown in figure 13 for the top (*b*), the middle (*c*) and the bottom (*d*) thermistor row. Solid symbols, ω_k; and open symbols, $\Delta\theta_k/\Delta t_{max}$. All data are for $Ra = 3.59 \times 10^{10}$ (run E16).

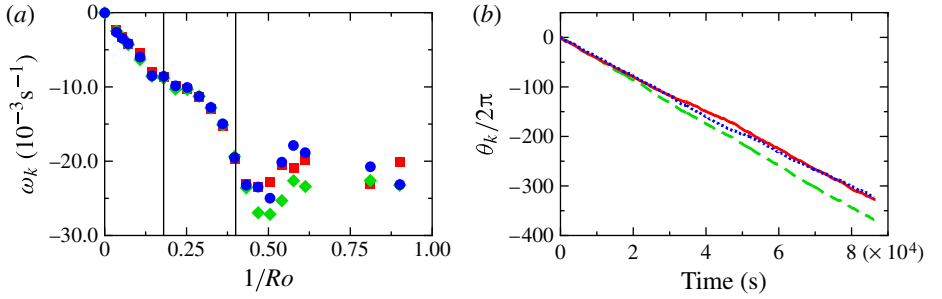

FIGURE 17. (Colour online) Rotation of the LSC for $\Gamma = 1$ and $Ra = 1.8 \times 10^{10}$ (run E8 of Zhong & Ahlers 2010). (*a*) LSC rotation rate as a function $1/Ro$ for top (bullets, blue online), the middle (diamonds, green online) and the bottom (squares, red online) thermistor row. The solid vertical lines mark the transition points at $1/Ro_0 = 0.18$ and $1/Ro_c = 0.4$. (*b*) θ_b (solid line, red online), θ_m (dashed line, green online) and θ_t (dotted line, blue online) as a function of time for $1/Ro = 0.47$.

clearly that $\dot{\theta}_m$ is larger than $\dot{\theta}_{b,t}$ when $1/Ro < 1/Ro_0$, as was seen before for ω_k. The faster rotation in the middle of the LSC is therefore not only due to the fact that $\langle\dot{\theta}_b\rangle$ and $\langle\dot{\theta}_t\rangle$ are reduced by 2π jumps while $\langle\dot{\theta}_m\rangle$ is not. Instead we believe that the jumps exist because the LSC is ripped apart once in a while due to a larger prograde rotation rate at the middle than at the top and bottom. This phenomenon is discussed in more detail in § 5.7. In general, the location of the maximum of $p(\dot{\theta}_k)$ as a function $1/Ro$ follows very closely the points of $\omega_k(1/Ro)$ from figure 13, as can be seen in figures 16(*b*)–(*d*). There one sees that ω_k and $\dot{\theta}_k$ differ very little from each other, with $|\dot{\theta}_k|$ slightly smaller that $|\omega_k|$.

For comparison, we re-analysed data for $\Gamma = 1$ that were previously published by Zhong & Ahlers (2010), using the straight-line fit to $\theta_k(t)$. Figure 17(*a*) shows a plot

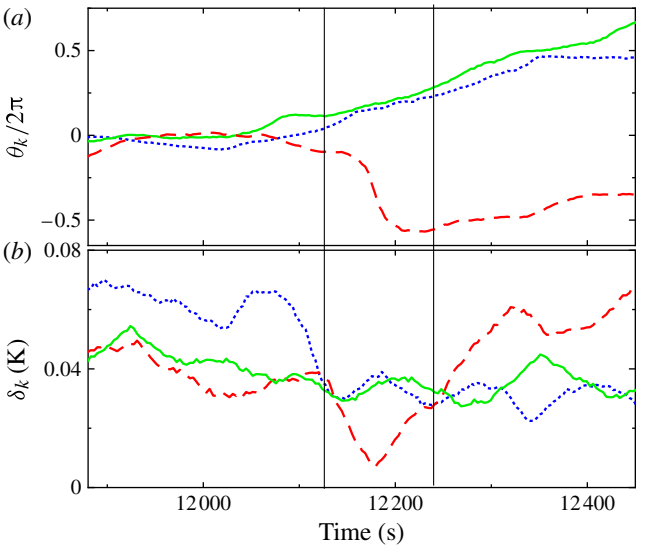

FIGURE 18. (Colour online) A short section of figure 14 that shows a half-turn. (*a*) Plots of θ_b (dashed, red online), θ_m (solid, green online) and θ_t (dotted, blue online) as a function of time. The data points are arbitrarily shifted by multiples of 2π. (*b*) Plots of δ_t (dotted, blue online), δ_b (dashed, red online) and δ_m (solid, green online) as a function of time. The vertical lines indicate the approximate times of the start and the finish of the half-turn.

similar to figure 13(*a*). It is consistent with figure 19(*a*) of Zhong & Ahlers (2010), but shows all three ω_k whereas the original work showed only ω_m. The direction of rotation and the monotonic behaviour as a function of $1/Ro$ is different from our finding for $\Gamma = 0.50$. The LSC rotates in the retrograde direction for all $1/Ro$ at a rate that monotonically becomes more negative as $1/Ro$ increases. Also, in contrast to figure 13(*a*), there is no difference between the rotation rates at the middle thermistor row and the top or bottom row as long as $1/Ro$ is smaller than 0.4. For $1/Ro > 0.4$ (i.e. beyond the second transition at $1/Ro_c$), the phase at the middle thermistor row starts to rotate faster than the top and bottom phases. This is also demonstrated in figure 17(*b*) which shows an example of the time evolution of θ_k. Also in this case a careful look revealed the existence of various 2π jumps for θ_t and θ_b that lead to a reduced ω_t and ω_b in comparison with ω_m.

5.7. *Half-turns and differential rotation*

To determine the reason for the jumps in $\theta_k(t)$ seen in figure 14, as well as earlier in figure 8, we plot θ_k and δ_k as a function of time for a single jump in figure 18. Note that the θ_k were shifted arbitrarily by multiples of 2π so that at the beginning of the plot all θ_k were close to zero. The LSC consisted of a SRS that had, however, a larger amplitude at the top than in the middle and at the bottom (figure 18*b*). An event started with a slight increase, followed by a decrease of δ_t. When δ_t reached the level of δ_m and δ_b, its decrease stopped while δ_b started to decrease. At the same time, θ_b decreased as well, while θ_m and θ_t continued to increase only very slightly. Here θ_b decreased until the difference between θ_b and the other θ_k reached 2π. In that time δ_b had reached a minimum, increased again above its value before the event started, and finally reached a value similar to the one that δ_t had before the event started.

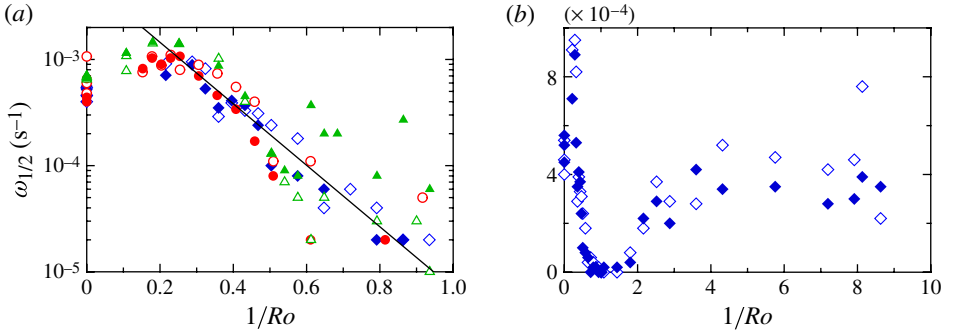

FIGURE 19. (Colour online) The frequency of half-turns ($\omega_{1/2}$) as a function of $1/Ro$. Open symbols mark half-turns that occur at the bottom part of the cell, solid symbols mark half-turns at the upper part of the cell. (*a*) $\omega_{1/2}$ on a vertical logarithmic scale and a narrow range of $1/Ro$ for $Ra = 1.8 \times 10^{10}$ (E15, diamonds, blue online), $Ra = 3.6 \times 10^{10}$ (E16, circles, red online) and $Ra = 7.2 \times 10^{10}$ (E17, triangles, green online). The solid line marks an exponential function with slope $m = 6.67$. (*b*) Only the data for $Ra = 1.8 \times 10^{10}$ (E15) on a vertical linear scale and a wide range of $1/Ro$.

Our interpretation of the above sequence of events is that the bottom part (less than a third or so) of the LSC became disconnected from the top part and quickly rotated in the retrograde direction for almost a full revolution until it became connected again with the top part to re-create a new SRS. We refer to such an event as a half-turn because half or less of the LSC underwent a rotation through 2π while the remainder more or less retained its original orientation. An alternative explanation could be given by considering small counter-rotating rolls that originate from corner flows and increase in size, similar to a flow-mode transition. However, as shown in figure 18, θ_b starts to deviate from θ_t and θ_m already before the corresponding amplitude δ_b decreases. This behaviour was also observed for other half-turns and is not in accord with a small counter-rotating roll emerging from the bottom. Half-turns can occur either in the top or in the bottom part of a SRS.

After a careful examination of the $\Gamma = 1$ data (Zhong & Ahlers 2010), we noted that similar half-turns also occurred for that case, albeit only for $1/Ro \gtrsim 1/Ro_c \simeq 0.4$ where θ_m rotated more rapidly in the retrograde direction than did the other two θ_k (see figure 17). We believe that these half-turns are one reason why the apparent cessation rate reported by Zhong & Ahlers (2010) increased with increasing $1/Ro$ when $1/Ro$ exceeded $1/Ro_c$.

In order to assess the importance of half-turns for $\Gamma = 0.50$ in various $1/Ro$ ranges, we defined an algorithm for their identification. A half-turn in the top part of the sample was assumed to have occurred when simultaneously $|\theta_t - \theta_m| > 2\pi/3$, $|\theta_b - \theta_m| < \pi/3$, $\delta_m > 0.15\langle\delta_m\rangle$ and $\delta_b > 0.15\langle\delta_b\rangle$. With a corresponding condition half-turns at the bottom part of the cell were identified. The results for the frequency of occurrence $\omega_{1/2}$ obtained with this algorithm are shown in figure 19. The left part shows $\omega_{1/2}$ on a logarithmic scale. It shows that half-turns occurred even for $1/Ro = 0$. Their frequency of occurrence increased slightly as $1/Ro$ grew, and after a maximum near $1/Ro = 0.2$ their frequency of occurrence became exponentially small near $1/Ro \simeq 1/Ro_c \simeq 0.8$. The right part of the figure gives $\omega_{1/2}$ on linear scales over a wider range of $1/Ro$ and shows that $\omega_{1/2}$, as defined by our algorithm, increased again near $1/Ro \simeq 2$ and reached a more or less constant value of about $\omega_{1/2} \approx 4 \times 10^{-4}$ s^{-1} at large $1/Ro$. If for $1/Ro \gtrsim 2$ the flow state is not actually a SRS of the LSC but rather a TVS, then we are measuring some dynamic property of this latter state which

also conforms to our algorithm. Elucidation of this issue by DNS would of course be most welcome. One might speculate that the apparent half-turns actually corresponded to vortex-length fluctuations of the TVS which occasionally exposed one or the other of $k = b$ or $k = t$ to only a single vortex; such a fluctuation would cause either δ_b or δ_t to become small while the other two amplitudes remained large.

We note that a possible partial explanation for the differential rotation was given by Kunnen (2008) and Kunnen *et al.* (2011). These authors observed, in DNSs for $\Gamma = 1$, $Ra = 1.0 \times 10^9$ and $Pr = 6.4$, an averaged azimuthal velocity for $1/Ro = 0.35$ near the horizontal midplane in the prograde direction while the averaged azimuthal velocity in the top and bottom portion of the sample rotated in the retrograde direction. As discussed above, the experiment yields only retrograde rotation and no differential rotation in this $1/Ro$ range for $\Gamma = 1$, but yields the unexpected prograde and differential rotation for $\Gamma = 0.50$. Kunnen *et al.* (2011) attributed the differential rotation, with $\omega_m > \omega_b$ and $\omega_m > \omega_t$, to the fact that the major axis of the LSC is tilted (Sun, Xi & Xia 2005*b*) with its long axis approximately along a diagonal in the near-vertical circulation plane. Near the horizontal midplane (where we measure θ_m) this tilt leads to a small velocity component in the radially inward direction. Since the angular momentum of this inward-moving fluid has to be conserved, they argue that the rotation rate has to increase while a fluid element is moving towards the centre. One should note, however, that the differential rotation observed by Kunnen *et al.* (2011) was observed in the averaged azimuthal velocity. Even though this quantity and the LSC are coupled, they are different properties of the system.

5.8. *The bend of the LSC for small* $1/Ro$

In figure 10 we already examined the probability distributions of $\Delta\theta_{b,t} \equiv \theta_b - \theta_t$ at two values of $1/Ro$. In order to understand the influence of the differential rotation discussed in § 5.7 on the structure and the dynamics of the LSC, we now consider in figure 20 the mean values $\langle \Delta\theta_{k_1,k_2} \rangle = \langle \theta_{k_1} - \theta_{k_2} \rangle$ of the differences between the three phases at the three different heights, and the corresponding r.m.s. deviations $\sigma(\Delta\theta_{k_1,k_2})$ from the mean values, as a function of $1/Ro$.

We consider first the left column of figure 20 which shows data for $\Gamma = 0.50$. The top row shows $\sigma(\Delta\theta_{k_1,k_2})$. It is not surprising that $\sigma(\Delta\theta_{t,b})$ (diamonds, green online) is larger than $\sigma(\Delta\theta_{t,m})$ or $\sigma(\Delta\theta_{b,m})$ because the vertical distance between the thermistor locations is twice as large, allowing for a weaker phase correlation. It is noteworthy that for all three $\Delta\theta_{k_1,k_2}$, the r.m.s. deviations $\sigma(\Delta\theta_{k_1,k_2})$ decrease continuously (after perhaps a small peak near $1/Ro \simeq 0.2$) with increasing $1/Ro$. This is consistent with the results shown above in figure 10.

There are three mechanisms that contribute to σ. These are first random fluctuations due to the stochastic nature of the turbulent flow, second the torsional motion of the LSC and third the flow-state transitions including the SRS–DRS–SRS transitions, half-turns, etc. A decrease of $\sigma(\Delta\theta_{k_1 k_2})$ indicates in general a stabilization of the single-roll LSC and a decrease of the intensity of its dynamics. The more detailed analysis of SRS–DRS–SRS transitions in § 5.3 already showed that the SRS was indeed stabilized by moderate rotation with respect to flow-state transitions, but moderate rotation also reduced the effect of random fluctuations as already shown in § 5.4.

The $\Gamma = 1$ case (right column of figure 20) looks different. Here all three σ values are closer together and have smaller values for $1/Ro = 0$. As for $\Gamma = 0.50$, they first decrease with increasing $1/Ro$, but then they reach a minimum near $1/Ro = 0.4 \simeq 1/Ro_c$ and increase again. In this case the decrease cannot be explained by a reduction of flow-mode transitions, since these transitions are very rare for $\Gamma = 1$.

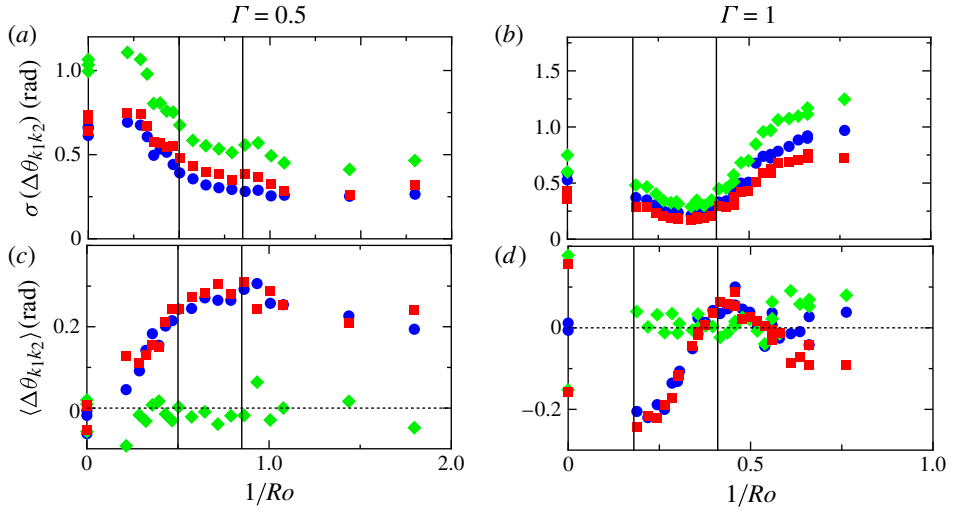

FIGURE 20. (Colour online) Statistics of the difference $\Delta\theta_{k_1,k_2}$. Top: standard deviation from its mean of $\Delta\theta_{mt}$ (bullets, blue online), $\Delta\theta_{b,t}$ (diamonds, green online) and $\Delta\theta_{m,b}$ (squares, red online). Bottom: average phase difference $\langle\Delta\theta_{m,t}\rangle$ (bullets, blue online), $\langle\Delta\theta_{b,t}\rangle$ (diamonds, green online) and $\langle\Delta\theta_{m,b}\rangle$ (squares, red online). Left: data for $\Gamma = 0.50$ and $Ra = 1.80 \times 10^{10}$ (run E15). Right: data for $\Gamma = 1.0$ and $Ra = 2.25 \times 10^{9}$ (run E6). The thin vertical lines indicate the location of $1/Ro_0$ (left) and $1/Ro_c$ (right). The horizontal dotted lines are drawn at $\langle\Delta\theta_{k_1,k_2}\rangle = 0$.

Therefore, either the amplitude of the torsional mode is damped by the rotation, or the random fluctuations are suppressed. However, the increases of σ for $1/Ro > 1/Ro_c$ may be explained by the strong increase of cessations or half-turns with increasing rotation rate as shown by Zhong & Ahlers (2010).

The lower two panels of figure 20 show the average $\langle\Delta\theta_{k1,k2}\rangle$ as a function of $1/Ro$ for $\Gamma = 0.50$ (*a*) and $\Gamma = 1.0$ (*b*). Let us focus first on the $\Gamma = 0.50$ case. Without rotation ($1/Ro = 0$), the average of all differences is close to zero. While $\langle\theta_t - \theta_b\rangle$ stays close to zero with increasing rotation, the phase differences between the top and the middle and between the bottom and the middle $\langle\theta_m - \theta_{t,b}\rangle$ increase with increasing rotation rate. The green curve ($\langle\theta_t - \theta_b\rangle$) does not give much information, since positive and negative values tend to average out and thus also a strong torsional mode would give a zero value. However, the blue and the red curves for $\langle\theta_m - \theta_{t,b}\rangle$ have surprisingly large values of the same sign that increase with increasing rotation rate. This fact cannot be explained by a torsional mode, since the periodic variation of $\Delta\theta_{m,t}$ and $\Delta\theta_{m,b}$ would also average to zero in the long run. Therefore, we have to assume that the LSC is bent, as shown in figure 21. The phase in the middle θ_m is on average larger than at the top and bottom. We believe that the reason for the bend is the same as that for the half-turns, i.e. a differential rotation that was observed already in simulations by Kunnen *et al.* (2011) for $\Gamma = 1$ but is found in experiment only for $\Gamma = 0.50$.

For $\Gamma = 1$ the situation is different. Also in that case there is a bend for small rotation rates $1/Ro \lesssim 1/Ro_c \simeq 0.4$, but this bend is in the opposite direction to what was seen for $\Gamma = 0.50$ as evidenced by the negative $\Delta\theta_{m,t}$ and $\Delta\theta_{m,b}$. At first sight this seems surprising because we saw in figure 17 that the rate of rotation was the same at all three levels, i.e. there is no evidence of any half-turns. A possible explanation

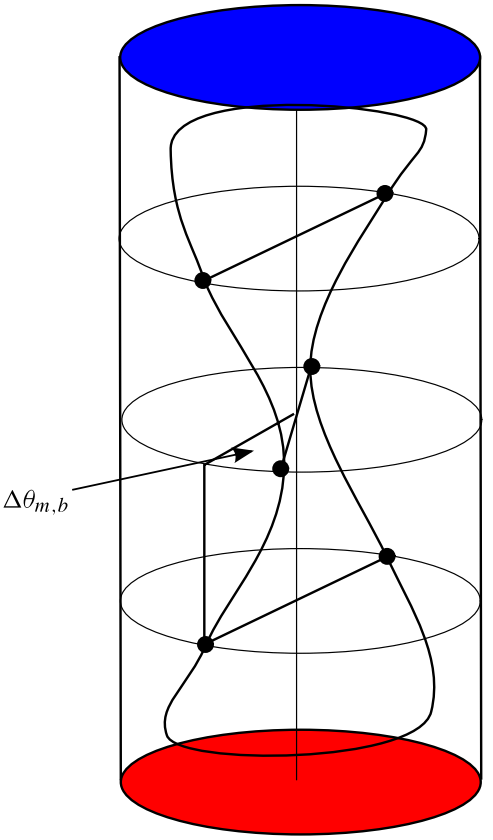

FIGURE 21. (Colour online) Sketch of the bent LSC due to rotation.

may be found in a difference of the frictional drag experienced by the LSC at different vertical positions. Near the top and bottom the rotation of the LSC in the inertial frame is caused by viscous drag along the sidewall as well as along the top or bottom plate, whereas the influence of the top/bottom plate is smaller or absent near the horizontal midplane of the sample. However, it is not obvious why this difference should vanish as $1/Ro$ approaches $1/Ro_c$. It is interesting to note that in the $\Gamma = 1$ case the bend apparently is not large enough to cause half-turns, and thus the local azimuthal velocities are the same everywhere.

As an alternative method for the study of the phase difference and the prograde rotation we computed cross-correlation functions of vertically adjacent sidewall temperature measurements for our $\Gamma = 0.50$ results. This approach avoided any fit of harmonic functions to, or Fourier analyses of, the sidewall temperatures. With this approach we could confirm not only the bend of the LSC, but we could also determine the rotation of the LSC relative to the container. We present this latter method of analysis and its results in the supplementary material associated with this paper (available at journals.cambridge.org/flm).

6. Summary

We presented a detailed investigation of the influence of rotation on turbulent thermal convection in a cylinder with aspect ratio $\Gamma = 0.50$ and with a fluid

of $Pr = 4.38$. For six different Rayleigh numbers in the range of $2.3 \times 10^9 \leqslant Ra \leqslant 7.2 \times 10^{10}$ we applied rotations with velocities up to $\Omega = 1$ rad s^{-1}, corresponding to inverse Rossby numbers $1/Ro$ up to $\sim$20.

Without rotation the LSC can consist of either a SRS or of a DRS where two rolls are positioned roughly one above the other. We found that modest rotation, corresponding to $1/Ro \lesssim 2$, stabilized the SRS and suppressed the DRS. We also investigated the average time that the system spent in the DRS and SRS and found that rotation increased the lifetime of the SRS and decreases that of the DRS. For larger $1/Ro$ a DRS-like signature re-appeared, but as discussed below, it probably was due to a vortex-flow structure rather than to a DRS.

The temperature gradient ΔT_w along the sidewall was measured as a function of $1/Ro$ and showed a behaviour similar to that observed for $\Gamma = 1$. At small $1/Ro$ it first decreased, but for $1/Ro \gtrsim 1/Ro_c \simeq 0.8$ it showed a strong increase. While the increase may have been due to an increasing suppression of vertical fluid transport due to rotation (i.e. due to the Taylor–Proudman effect), the origin of the original decrease of ΔT_w is less clear.

Criteria based on a Fourier analysis suggested by Stevens *et al.* (2011*a*) were used to attempt to establish the $1/Ro$ range of the existence of the LSC. This analysis suggested that the LSC existed up to our largest $1/Ro$. However, the criteria available to us cannot distinguish between a LSC consisting of a convection roll on the one hand and a TVS on the other. In the TVS one vortex extends vertically from the top into the sample interior and brings down cold fluid, while another emanates from the bottom and introduces warm fluid. The net result is a periodic azimuthal temperature variation which cannot be distinguished from the temperature signature of a convection roll with upflow and downflow near the sidewall but separated azimuthally by π. A TVS was found before from DNS by Stevens *et al.* (2011*b*) for $\Gamma = 1/2$, $1/Ro = 3.33$, $Pr = 4.38$ and $Ra = 2.91 \times 10^8$, but its prevalence over wide ranges of Pr, $1/Ro$ and Ra was unknown. It seems likely that our measurements of the dynamical properties of the system for $1/Ro \gtrsim 2$ really pertain to the TVS, and that for those inverse Rossby numbers the TVS existed over our parameter ranges.

For comparison we re-analysed data for $\Gamma = 1$ of Zhong & Ahlers (2010). Although moderate rotation stabilized the LSC also in this case, we found that the LSC signature disappeared soon after $1/Ro$ exceeded $1/Ro_c \simeq 0.4$. This is consistent with the fact that the larger cross-section of the sample would contain more than two Ekman vortices which would lead to a more complicated azimuthal temperature signature.

Without rotation it had been noted for $\Gamma = 0.50$ that the amplitude of the LSC measured at one of the three vertical positions frequently vanished (Xi & Xia 2008*b*; Weiss & Ahlers 2011*b*). We called these dips events. At moderate rotation the frequency of the events decreased with increasing $1/Ro$, reached a minimum at around $1/Ro \approx 1$, and increases again for larger rotation rates where the TVS may have existed. In the LSC parameter range events are caused by SRS–DRS–SRS transitions as well as by so-called half-turns. During a half-turn, a part of the SRS of the LSC at the bottom or the top decouples from the rest and rotates around the cylinder axis in opposite direction to the rest. The rotation ends when both parts are in phase again and the original single roll is reinstated.

For $\Gamma = 0.50$ half-turns were caused by a differential rotation of the LSC that was observed for small rotation rates ($1/Ro < 1/Ro_0$). For $\Gamma = 1$ the LSC plane rotated in the retrograde direction in the frame of the sample; in contrast to that the LSC plane rotated in the prograde direction for $\Gamma = 0.50$ and $1/Ro \lesssim 1$, i.e. in the same

rotation direction as and faster than the container. The origin of this phenomenon is unclear. An additional interesting phenomenon is that the fluid rotated faster in the horizontal midplane of the cylinder than it did closer to the top and bottom plates. This differential rotation could be seen by looking at the probability distributions of the instantaneous rotation rates $\mathrm{d}\theta/\mathrm{d}t$ of the LSC at the three different heights. In addition to causing half-turns, the differential rotation also had the effect of bending the LSC so that a positive phase difference existed between θ_m on the one hand and θ_b and θ_t on the other. The phase difference and the prograde rotation could also be observed in the cross-correlation functions of vertically adjacent thermistors. With this approach we could confirm not only the bend of the LSC, but we could also determine the rotation of the LSC relative to the container. We present this latter method of analysis in a document submitted as supplementary material.

We benefitted form numerous stimulating discussions with Hermann Clercx, Detlef Lohse and Richard Stevens. We are especially grateful to Richard Stevens for calling our attention to the two-vortex state and its possible relevance to our flow-structure determinations. This work was supported by NSF grant DMR07-02111.

Supplementary material is available at journals.cambridge.org/flm

REFERENCES

AHLERS, G. 2009 Turbulent convection. *Physics* **2**, 74-1–7.

AHLERS, G., GROSSMANN, S. & LOHSE, D. 2009 Heat transfer and large scale dynamics in turbulent Rayleigh–Bénard convection. *Rev. Mod. Phys.* **81**, 503–538.

BAILON-CUBA, J., EMRAN, M. & SCHUMACHER, J. 2010 Aspect ratio dependence of heat transfer and large-scale flow in turbulent convection. *J. Fluid Mech.* **655**, 152–173.

BROWN, E. & AHLERS, G. 2006*a* Effect of the Earth's Coriolis force on turbulent Rayleigh–Bénard convection in the laboratory. *Phys. Fluids* **18**, 125108.

BROWN, E. & AHLERS, G. 2006*b* Rotations and cessations of the large-scale circulation in turbulent Rayleigh–Bénard convection. *J. Fluid Mech.* **568**, 351–386.

BROWN, E. & AHLERS, G. 2007 Temperature gradients, and search for non-Boussinesq effects, in the interior of turbulent Rayleigh–Bénard convection. *Europhys. Lett.* **80**, 14001.

BROWN, E. & AHLERS, G. 2008*a* Azimuthal asymmetries of the large-scale circulation in turbulent Rayleigh–Bénard convection. *Phys. Fluids* **20**, 105105.

BROWN, E. & AHLERS, G. 2008*b* A model of diffusion in a potential well for the dynamics of the large-scale circulation in turbulent Rayleigh–Bénard convection. *Phys. Fluids* **20**, 075101.

BROWN, E. & AHLERS, G. 2009 The origin of oscillations of the large-scale circulation of turbulent Rayleigh–Bénard convection. *J. Fluid Mech.* **638**, 383–400.

BROWN, E., NIKOLAENKO, A. & AHLERS, G. 2005 Reorientation of the large-scale circulation in turbulent Rayleigh–Bénard convection. *Phys. Rev. Lett.* **95**, 084503.

CILIBERTO, S., CIONI, S. & LAROCHE, C. 1996 Large-scale flow properties of turbulent thermal convection. *Phys. Rev.* E **54**, R5901–R5904.

DU, Y. B. & TONG, P. 2000 Turbulent thermal convection in a cell with ordered rough boundaries. *J. Fluid Mech.* **407**, 57–84.

FUNFSCHILLING, D. & AHLERS, G. 2004 Plume motion and large scale circulation in a cylindrical Rayleigh–Bénard cell. *Phys. Rev. Lett.* **92**, 194502.

FUNFSCHILLING, D., BROWN, E. & AHLERS, G. 2008 Torsional oscillations of the large-scale circulation in turbulent Rayleigh–Bénard convection. *J. Fluid Mech.* **607**, 119–139.

FUNFSCHILLING, D., BROWN, E., NIKOLAENKO, A. & AHLERS, G. 2005 Heat transport by turbulent Rayleigh–Bénard convection in cylindrical cells with aspect ratio one and larger. *J. Fluid Mech.* **536**, 145–154.

HART, J. E., KITTELMAN, S. & OHLSEN, D. R. 2002 Mean flow precession and temperature probability density functions in turbulent rotating convection. *Phys. Fluids* **14**, 955–962.

JULIEN, K., LEGG, S., MCWILLIAMS, J. & WERNE, J. 1996 Rapidly rotating turbulent Rayleigh–Bénard convection. *J. Fluid Mech.* **322**, 243–273.

KING, E., STELLMACH, S., NOIR, J., HANSEN, U. & AURNOU, J. 2009 Boundary layer control of rotating convection systems. *Nature* **457**, 301–304.

KUNNEN, R. P. J. 2008 Turbulent rotating convection. PhD thesis, University of Eindhoven.

KUNNEN, R. P. J., CLERCX, H. J. H. & GEURTS, B. J. 2008 Breakdown of large-scale circulation in turbulent rotating convection. *Europhys. Lett.* **84**, 24001.

KUNNEN, R. P. J., GEURTS, B. J. & CLERCX, H. J. H. 2010 Experimental and numerical investigation of turbulent convection in a rotating cylinder. *J. Fluid Mech.* **642**, 445–476.

KUNNEN, R. P. J., STEVENS, R. J. A. M., OVERKAMP, J., SUN, C., VAN HEIJST, G. & CLERCX, H. J. H. 2011 The role of Stewartson and Ekman layers in turbulent rotating Rayleigh–Bénard convection. *J. Fluid Mech.* **688**, 422–442.

LIU, Y. & ECKE, R. 2009 Heat transport measurements in turbulent rotating Rayleigh–Bénard convection. *Phys. Rev.* E **80**, 036314.

LOHSE, D. & XIA, K.-Q. 2010 Small-scale properties of turbulent Rayleigh–Bénard convection. *Annu. Rev. Fluid Mech.* **42**, 335–364.

MALKUS, M. V. R. 1954 The heat transport and spectrum of thermal turbulence. *Proc. R. Soc. Lond.* A **225**, 185–195.

NIKOLAENKO, A., BROWN, E., FUNFSCHILLING, D. & AHLERS, G. 2005 Heat transport by turbulent Rayleigh–Bénard convection in cylindrical cells with aspect ratio one and less. *J. Fluid Mech.* **523**, 251–260.

ROSSBY, H. T. 1969 A study of Bénard convection with and without rotation. *J. Fluid Mech.* **36**, 309–335.

STEVENS, R., CLERCX, H. J. H. & LOHSE, D. 2011*a* Effect of plumes on measuring the large scale circulation in turbulent Rayleigh–Bénard convection. *Phys. Fluids* **23**, 095110.

STEVENS, R. J. A. M., CLERCX, H. J. H. & LOHSE, D. 2010 Boundary layers in rotating weakly turbulent Rayleigh–Bénard convection. *Phys. Fluids* **22**, 085103.

STEVENS, R. J. A. M., OVERKAMP, J., LOHSE, D. & CLERCX, H. J. H. 2011b Disappearance of aspect ratio dependence of heat transport with increasing rotation rate in turbulent Rayleigh–Bénard convection. *Phys. Rev.* E (in press).

STEVENS, R. J. A. M., ZHONG, J., CLERCX, H. J. H., AHLERS, G. & LOHSE, D. 2009 Transitions between turbulent states in rotating Rayleigh–Bénard convection. *Phys. Rev. Lett.* **103**, 024503.

SUN, C., REN, L.-Y., SONG, H. & XIA, K.-Q. 2005*a* Heat transport by turbulent Rayleigh–Bénard convection in cylindrical cells of widely varying aspect ratios. *J. Fluid Mech.* **542**, 165–174.

SUN, C., XI, H. D. & XIA, K. Q. 2005*b* Azimuthal symmetry, flow dynamics, and heat transport in turbulent thermal convection in a cylinder with an aspect ratio of 0.5. *Phys. Rev. Lett.* **95**, 074502.

TILGNER, A., BELMONTE, A. & LIBCHABER, A. 1993 Temperature and velocity profiles of turbulence convection in water. *Phys. Rev.* E **47**, R2253–R2256.

TRITTON, D. J. 1988 *Physical Fluid Dynamics*. Oxford University Press.

VAN DER POEL, E., STEVENS, R. J. A. M. & LOHSE, D. 2011 Connecting flow structures and heat flux in turbulent Rayleigh–Bénard convection. *Phys. Rev.* E **84**, 045303.

WEISS, S. & AHLERS, G. 2011a Heat transport by turbulent rotating Rayleigh–Bénard convection. *J. Fluid Mech.* (in press).

WEISS, S. & AHLERS, G. 2011*b* Turbulent Rayleigh–Bénard convection in a cylindrical container with aspect ration $\Gamma = 0.50$ and Prandtl number $\mathrm{Pr} = 4.38$. *J. Fluid Mech.* **676**, 5–40.

WEISS, S., STEVENS, R., ZHONG, J.-Q., CLERCX, H., LOHSE, D. & AHLERS, G. 2010 Finite-size effects lead to supercritical bifurcations in turbulent rotating Rayleigh–Bénard convection. *Phys. Rev. Lett.* **105**, 225401.

XI, H.-D. & XIA, K.-Q. 2007 Cessations and reversals of the large-scale circulation in turbulent thermal convection. *Phys. Rev.* E **75**, 066307.

XI, H.-D. & XIA, K.-Q. 2008*a* Azimuthal motion, reorientation, cessation, and reversals of the large-scale circulation in turbulent thermal convection: a comparative study in aspect ratio oner and one-half geometries. *Phys. Rev.* E **78**, 036326.

XI, H.-D. & XIA, K.-Q. 2008*b* Flow mode transition in turbulent thermal convection. *Phys. Fluids* **20**, 055104.

XI, H.-D., ZHOU, S.-Q., ZHOU, Q., CHAN, T.-S. & XIA, K.-Q. 2009 Origin of the temperature oscillation in turbulent thermal convection. *Phys. Rev. Lett.* **102**, 044503.

XIA, K.-Q. & LUI, S.-L. 1997 Turbulent thermal convection with an obstructed sidewall. *Phys. Rev. Lett.* **79**, 5006–5009.

XU, X., BAJAJ, K. M. S. & AHLERS, G. 2000 Heat transport in turbulent Rayleigh–Bénard convection. *Phys. Rev. Lett.* **84**, 4357–4360.

ZHONG, J.-Q. & AHLERS, G. 2010 Heat transport and the large-scale circulation in rotating turbulent Rayleigh–Bénard convection. *J. Fluid Mech.* **665**, 300–333.

ZHONG, J.-Q., STEVENS, R. J. A. M., CLERCX, H. J. H., VERZICCO, R., LOHSE, D. & AHLERS, G. 2009 Prandtl-, Rayleigh-, and Rossby-number dependence of heat transport in turbulent rotating Rayleigh–Bénard convection. *Phys. Rev. Lett.* **102**, 044502.

ZHOU, Q., XI, H.-D., ZHOU, S.-Q., SUN, C. & XIA, K.-Q. 2009 Oscillations of the large-scale circulation in turbulent Rayleigh–Bénard convection: the sloshing mode and its relationship with the torsional mode. *J. Fluid Mech.* **630**, 367–390.